2007

Selective laser sintering of stearic acid-coated alumina ceramic

Jason J. Nolte

Department:

SELECTIVE LASER SINTERING OF STEARIC ACID-COATED ALUMINA CERAMIC

by

JASON JOHN NOLTE

A THESIS

Presented to the Faculty of the Graduate School of the

UNIVERSITY OF MISSOURI-ROLLA

In Partial Fulfillment of the Requirements for the Degree

MASTER OF SCIENCE IN MECHANICAL ENGINEERING

2007

Approved by

_____	_____
Dr. Ming C. Leu, Advisor	Dr. Greg E. Hilmas

_____

Dr. Frank W. Liou

ABSTRACT

The purpose of this research is to develop a process that will enable a Selective Laser Sintering (SLS) machine to create geometrically complex green parts of various sizes that become strong, dense ceramic parts after sintering. This will be applicable to SLS systems already operational in industry, and may offer a more cost-effective, more time-efficient method for producing high-temperature ceramic rapid prototype parts.

Alumina was the chosen ceramic for the developmental stage of this research. Fine alumina powder (average particle size of 0.4 μm) was coated with stearic acid, which served as a binder. Green parts were made from this powder using low temperature, low laser power SLS processes. The green strength of parts produced in this research was sufficient for safe transport and to survive the binder burnout process to remove the organic binder. The average final density of fully sintered parts was 88% of the theoretical density for alumina (3.96 g/cm^3), and the average flexural strength of fully sintered flexural test bars was 255 MPa. The sintered parts have an average surface roughness of approximately 7.6 μm without any finishing processes such as grinding or polishing. No infiltration, compaction, or post-processing other than binder burnout/sintering is required to achieve these results.

Holes of diameters less than 1 mm and holes with multiple bends have consistently been produced in Al_2O_3 parts of various thickness and height. Average dimensional variances are approximately 0.12 mm for hole diameters and 0.25x0.27x0.21 mm for the length, width, and height of flexural strength bars, respectively. Features of green parts produced in this research include sharp corners, crisp lines, flat surfaces, complex holes, slots, and overhangs.

ACKNOWLEDGMENTS

My thanks goes to my advisor, Dr. M. Leu, and to the members of the CAMT group, Drs. G. Hilmas, F. Dogan, and R. Landers, that have generously granted me their guidance and support for this wonderful research opportunity. The CAMT is wisely funded by the Air Force Research Laboratory under contract FA8650-04-C-5704. I am privileged to work with such a distinguished group of intelligent people.

I also thank the members of my thesis committee, Drs. M. Leu, G. Hilmas, and F. Liou, for their attentive interest in and approval of this project's documentation and presentation. Without it, I would not be able to graduate.

My thanks also goes to Mike Hayes and David Dietrich of the Boeing Company who have dedicated time and resources to supply technical support to the research. The quality of this project would not have been as good without their assistance.

I also thank Dr. Zhehui Liu and Dr. Tieshu Haung for their material expertise and patient explanations. Thank you Tom Hudson, Ian Packard, Erik Adamek, Karteek Kesavamatham, Mike Mason, Fu Qiang, and everyone else who aided in the advancement of this project.

My thanks and love go out to my wife, Natalie, for having the patience, tolerance, and understanding to help me through graduate school. She has given me more than I will ever fully realize.

Thanks also goes to all of my friends who have encouraged me, through their own thesis experience, to start writing early, to write often, and to edit thoroughly.

I am blessed to interact with and have the support of all of the people and orginizations mentioned above.

TABLE OF CONTENTS

LIST OF ILLUSTRATIONS

LIST OF TABLES

1. INTRODUCTION

1.1. HIGH-TEMPERATURE CERAMIC PROCESSING

The use of high-temperature ceramics has been of great interest in several industries including aerospace, consumer electronics, power generation, and chemical processing. The fact that ceramic materials tend to be able to withstand high temperatures, are chemically inert, and have high strength and stiffness characteristics makes ceramics ideal in some situations where other materials, such as metals and polymers, are not. Manufacturing dense parts from these materials using conventional techniques requires a lot of time and resources.

One common method used to produce parts of complex geometries from high-temperature ceramics is to press a binder-coated ceramic powder into a mold. Heat is usually applied to fuse the binder coatings together. This creates a green part (part made of binder-coated ceramic) in the shape of the desired geometry. The green part is later sintered in a furnace to remove the binder (forming a brown part). The brown part is then placed in a high-temperature furnace to sinter the ceramic particles together, which brings the part to its final density. This is a cumbersome process that can produce parts with high densities ($\geq$ 98% relative density), but has several drawbacks such as geometric limitations, lengthy time-to-production due to mold fabrication, and high cost – especially for low production volume parts – to pay for mold machining time and part processing.

1.2. RAPID PROTOTYPING TECHNOLOGIES

Rapid prototyping involves the creation of a dimensionally accurate part directly from a computer model of a part. There are several different methods to produce such parts from computer-aided design (CAD) models. Examples of common rapid prototyping (RP) processes are stereolithography (SLA), fused deposition modeling (FDM), and selective laser sintering (SLS). All of these require that CAD files be sliced into sections that can be electronically loaded into a controller for a laser scanner or material deposition system.

SLA creates a part from a liquid resin that cures when exposed to an ultraviolet light source. The process was one of the initial RP modeling machines to be mass produced and widely available to industry. The CAD model of the part is broken into several sections or layers. Each layer is scanned by a UV laser onto the surface of the liquid, which cures the liquid to form a solid part. Upon the completion of the scanning, the build table moves down or up one layer thickness in the liquid reservoir and then the cycle repeats.

SLA offers a smooth, glass-like surface finish on flat part surfaces oriented in the machine's X-Y plane. The SLA process is accurate to 0.001 to 0.003 in, better than the FDM and SLS processes by at least 0.001 in. However, because of the relative uniqueness of the liquid, material options are limited. Figure 1.1 shows some examples of parts produced by SLA [31]. Figure 1.2 shows an operational diagram of one type of SLA machine [23].

FDM is a popular form of RP that uses a polymer in pellet form or as a spool of chord that is fed into the machine. Most parts made in this process require overhangs and

Figure 1.1: SLA part examples

holes to be made with a support material to help ensure part strength during fabrication. Chord from the spool is pushed through a heated nozzle that deposits a thin bead of material (usually a plastic of some kind). ABS and polycarbonate are two examples of common materials used in this RP technology. Figure 1.3 shows a diagram of the basic

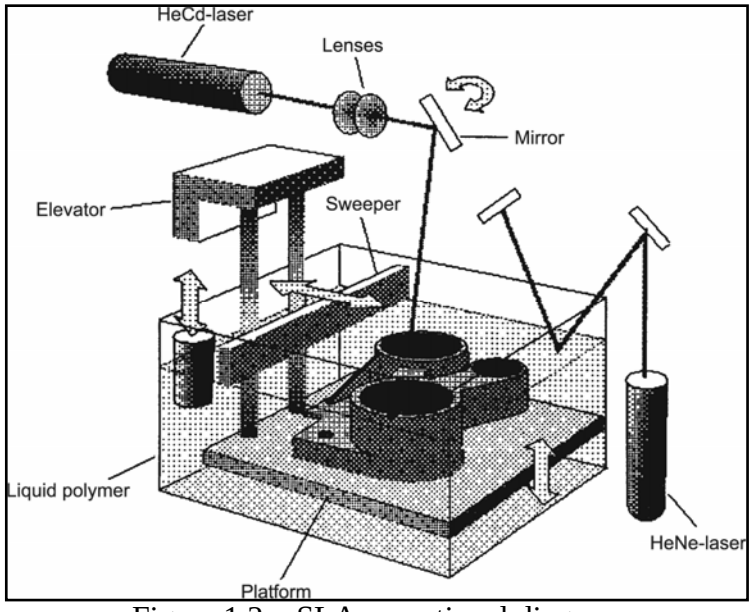

Figure 1.2: SLA operational diagram

FDM components [28]. Figure 1.4 shows a magnified cross-section of a part made by FDM [1]. The polymer strands are the lighter colored areas, and the dark areas are voids in the part. The initial surface finish is not as smooth as SLA, but in most cases a blend of material is possible to obtain desired visual and structural affects. The accuracy of the FDM process ranges from 0.003 to 0.005 inches.

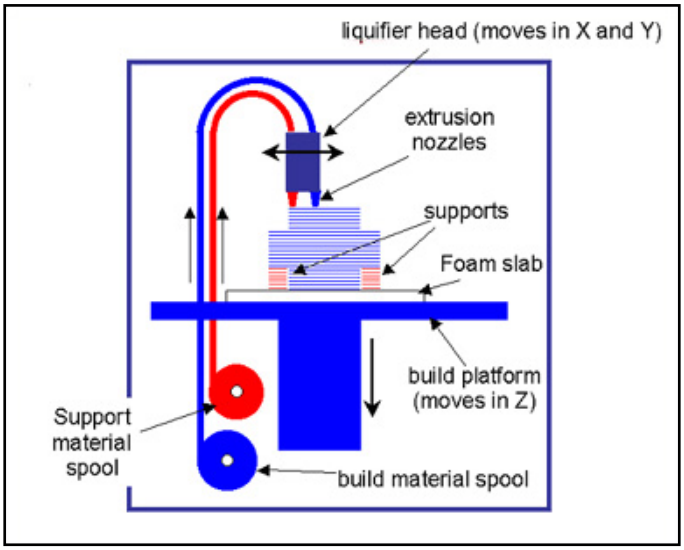

Figure 1.3: Diagram of the basic components of an FDM process and part

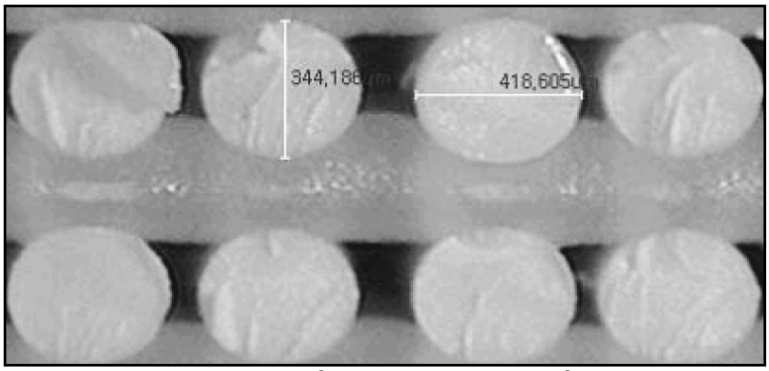

Figure 1.4: Magnified cross section of FDM part

1.3. SELECTIVE LASER SINTERING

Selective Laser Sintering (SLS) was originally developed by the University of Texas between 1987 and 1989 as a laser based rapid prototyping technology for polymers. The principle employs a high-powered CO_2 laser ($\geq$ 50 W) to sinter finely crushed polymer powder (typical average particle size ranges from 50 to 150 μm). A three-dimensional STL model of the part to be produced is sliced into layers of a specified thickness. The contours of the first layer are electronically transferred to the laser controller, which moves galvo mirrors to outline and fill in the slice profile. After the first layer is completed, the build area lowers one layer thickness and fresh powder is spread over the sintered profile. The process repeats itself with the scanning of a new layer until the entire part is sintered. The loose, non-sintered powder surrounding the sintered profile acts as support material for part features. After the build, the part cake must be removed and the desired parts must be "broken out" of the part cake after it is removed from the machine. This could involve something as mild as blowing the powder away with low-pressure air or something as abrasive as sandblasting. Figure 1.5 shows an operation diagram for a SLS machine [33]. Figure 1.6 shows an example of SLS parts produced in-house.

To avoid confusion with use of the term "sintering", in this document, the act of joining two powder particles together using an SLS machine shall be noted as "fusing" and the use of a furnace to join independent ceramic particles shall be called "sintering". In other words, to create ceramic green parts, the SLS machine fuses the binder coatings together, and the ceramic parts are sintered after the binder burnout process in a high-temperature furnace.

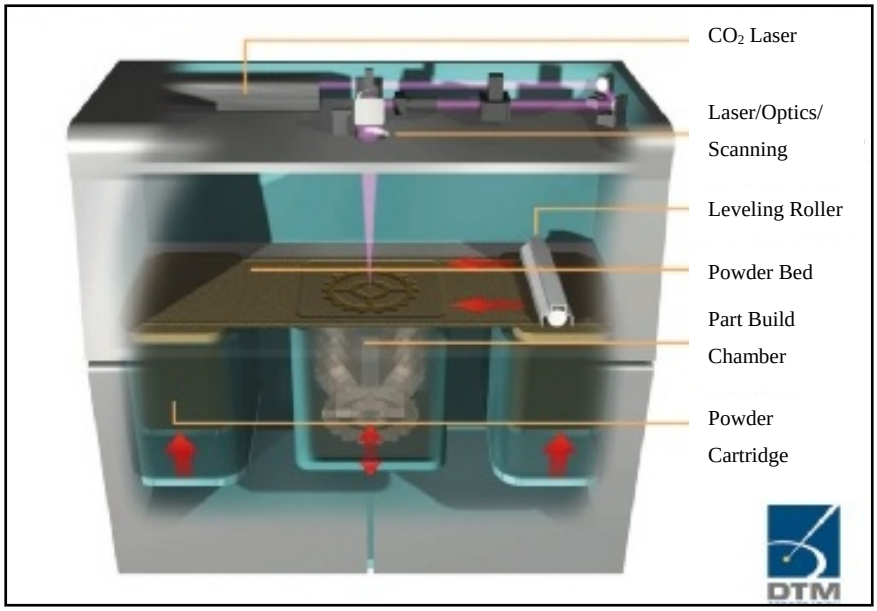

Figure 1.5: The SLS operation diagram

Figure 1.6: SLS parts – 5 independent, free-spinning balls in one made at UMR

1.4. POTENTIAL APPLICATIONS

The ability to combine the geometric capabilities of the SLS process with the material properties of ceramics has been a long interest of several research endeavors. Several limits of current manufacturing techniques could be overcome with a manufacturing process like SLS. The benefit of this technology would not be as notable

if the green parts required extensive post-processing. In a marketplace where time is money, the turnaround time for products from conception to production must be as small as possible. There exist several techniques to improve the properties of green parts, infiltration for example, but each process requires a larger investment in post-processing equipment and time. The ideal process would require only the sintering process to produce the final parts from the green parts. Powder would also have to be readily available for industrial consumption. Also, a simple powder production procedure is desirable to effectively meet the varying demands of industry.

Keeping these things in mind, this research sought to develop a powder that was simple, quick, and safe to produce that would work well in SLS machines without requiring any modification. Another goal for this powder was to enable green parts of sufficient strength for safe transport and successful binder burnout to be produced by SLS. The level of geometric accuracy (approximately 0.003 in) currently available from standard SLS processes using standard materials, such as Duraform™, was desirable for the ceramic green parts as well.

1.5. OVERVIEW OF THESIS

Following this introduction is Section 2, a literature review that examines previous attempts to accomplish goals similar to those of this research. It also provides a more in-depth review of current ceramic part production techniques. Section 3, the experimentation section, lists the equipment and experimental setups used to conduct this research. Section 4 contains the discussion of the results achieved in the experimentation. The conclusions are stated and briefly discussed in Section 5. Then

future areas of interest for this research are mentioned in Section 6. To conclude this thesis, references are listed and supplemental information is included in the appendix sections.

2. LITERATURE REVIEW

2.1. PREVIOUS WORK WITH SLS OF CERAMICS

Several attempts have been made to produce ceramic parts using SLS technologies. The approach taken by most research projects, as it is in this thesis study, is to coat ceramic particles with a binder that can be melted during the SLS process. The selection of the binder is usually the primary element that determines the success of the project. Other key issues are ceramic particle size, post SLS binder burnout and sintering procedures, and the SLS parameter values to produce the green parts.

Experimentation using SLS technology to make ceramic parts has been conducted since the early 1990's. One early example is J. C. Nelson's use of SLS to create green parts of a polymer-coated silicon carbide powder (SiC) [17]. While successful parts were made, porosity was an issue. It was observed that the green parts were as porous as the powder bed they were sintered in (approximately 50% by volume). These parts used PMMA (polymethyl methacrylate) for a binder and had a SiC particle size range of 2 to 60 μm. After encapsulation, the average particle size was less than 50 μm. In other studies, particle size was found to be an important factor in producing successful ceramic green parts using SLS; the smaller the particle, the better for sintering processes [18, 11].

Subramanian created alumina parts using an SLS process by coating ceramic particles with polymer binders, but the maximum strength achieved was only 14 MPa. The corresponding density for those results was reported to be only 55% of the maximum theoretical density [22]. An attempt was made to make Si/SiC composites using a binder-coated SiC powder and SLS. The reported average strength of the parts after

infiltration was 70 MPa [21]. An approximate range of flexural strengths of dense SiC parts is 400 to 550+ MPa depending on part purity and density.

A more recent attempt to make high quality SiC parts using tailored SLS and sintering techniques was performed by Bourell, et al. [2]. This process also required the green part to be infiltrated with silicon during the sintering process to increase the part strength and density to the desired levels. In addition to parts warping, silicon accumulation on surfaces, particularly in corners, was an important issue that needs to be resolved before parts reach the desired quality. This research sought to create a high-temperature ceramic part using the SLS process that does not require infiltration to obtain specific mechanical characteristics. Due to the inherent porosity of the parts produced by the SLS process (approximately 50%), this is a challenging task.

Another attempt to use SLS technology to fabricate Si/SiC ceramic parts produced similar results [14]. Green parts were producible and required infiltration to achieve maximum densities (~ 52%). The parts were also of low relative strength, 195MPa, when compared to the typical 350 MPa from dense (≥97%) parts.

Several attempts to use traditional SLS parts made of nylon to serve as molds for casting ceramic parts have met reasonable success. Guo et al. [7] utilized this principle to create complex shapes out of PZT (lead zirconate titanate). The polymer mold is burnt out during sintering. The intentions of the research discussed in this thesis was to find a material and process that enabled green ceramic part to be directly created from the SLS process and then sintered to create dense ceramic parts.

2.2. PREVIOUS WORK WITH FREEFORM FABRICATION OF CERAMICS

Solid freeform fabrication (SFF) techniques were originally developed for the fabrication of polymer parts to check design form and fit. The fabrication of dimensionally accurate, complex 3D parts that require no machining or tooling remains an attractive option for the production of ceramic parts. SFF techniques have the potential for reducing the time-to-production and cost per part for low-production-volume parts by eliminating the time and cost it takes to create molds for ceramic parts. In addition to SLS, several other freeform fabrication techniques have been used to produce ceramic parts with varying degrees of success. Extrusion-based technologies, such as extrusion freeform fabrication (EFF), layer-wise slurry deposition (LSD), and freeze-form extrusion fabrication (FEF) are three methods being used in experimentation. An experimental SLA process has also been created to explore that process's potential for producing ceramic parts.

2.2.1. Extrusion Freeform Fabrication. One of the advantages of FDM rapid prototyping technologies is that the process requires little excess material (only support material for geometric features like overhangs) be used to stably create parts. One approach to utilizing the FDM process for ceramic part fabrication is to modify an existing FDM machine with a high-pressure extruder head to extrude green ceramic feed-rod. One such machine (called an EFF machine) has been used to create functional ceramic parts [24]. In this research, a binder-coated ceramic (Si_3N_4) feed-rod with a 55 vol % solids loading was loaded into the feed for the machine. Sintered ceramic parts were reported to be greater than 97% dense and shrank 20% ± 5% in the Z-direction and 18% ± 3% in the XY-plane. The disadvantages of EFF process are in the sensitive

material preparation. The binder consists of polymers, waxes, and plasticizers. If not mixed in proper ratios and uniformly, the material will not extrude properly in the EFF machine. Improper mixing also could result in weak green and sintered parts as well as distorted brown and sintered parts. Also, the feed-rods are stiff and have finite lengths (152.4mm in this research). This limits the size of part that can be produced, and if multiple feed rods were used in a build, the gap between the two rods cause dimensional inaccuracies and part instability due to gaps in material flow.

Dental ceramics have taken particular interest in SFF of ceramic parts for the quick turnaround time and low cost to make teeth as individualistic as the people in which they are implanted. A micro-extrusion process was used in conjunction with pseudo-plastic porcelain slurry that allowed for low-pressure, dimensionally accurate extrusion [25]. A green tooth could be fabricated in 30 minutes or less using the methods discussed in this research. The green teeth were allowed to dry in air, during which the parts shrank approximately 3% in each direction. During the sintering process, part shrinkages averaged 27% in the build direction and 24% in the build plane. Surface roughness of the parts ranged from 20 to 50 µm, which is not as good as other SFF processes, like SLS.

2.2.2. Layer-Wise Slurry Deposition. Another method used for rapid dental ceramic part fabrication combines the functionality principles of tape-casting and SLS technologies [5]. Similar to tape-casting, a doctor blade is used to deposit and smooth a layer of slurry over a build area. After a layer is deposited (~ 100 µm thick), the laser scans the desired geometric profile from the sliced CAD part. The slurry undergoes reaction sintering to form mullite, which is necessary for the mechanical

stability of green parts. After that, the build platform lowers and the process repeats. The slurry consists of Al_2O_3-SiO_2 and water. For this research, the solids loadings were varied over a range from 63 to 87 wt % of Al_2O_3-SiO_2 mix. The optimum material ratios were determined to be 68.5 wt% amorphous silica, 25.5 wt% alumina, and 6.0 wt% water. The part still required further sintering for densification. The densities of the ceramic parts varied between 86 and 92 % of the theoretical density (2.39 g/cm^3). In poreless sections of parts built in this research, the maximum surface roughness was 4.6 μm. The open porosity of parts ranged from 10% to 14%. The maximum pore diameter was 30 μm. Shrinkages in the XY-plane were on average 2%, and shrinkages averaged 10% in the Z-direction. Lack of material versatility is a hindrance of this process. There were reported problems with inconsistent bonding between layers. The materials available for this process are very limited in comparison with other ceramic SFF process.

2.2.3. Freeze-Form Fabrication. Another concern of the ceramic industry is the environmental effects of using organic binders, which, when burnt out of the green part, can release carbon monoxide among other harmful gases into the atmosphere. One such solution is to use water as the primary media to form ceramic slurries [10]. Alumina solids loading as high as 60 vol. % have been achieved in the slurries for this process [15]. Parts are made using a custom-built machine that has a ram for material extrusion. Parts can be fabricated at room temperature or in a cooled environment to improve green strength, which is necessary for the fabrication of large green parts. After fabrication, the parts are freeze-dried prior to sintering to remove some of the water from the samples (~ 30%). The binder is then fully removed in a furnace and the parts are then sintered to obtain ~ 90.5% theoretical densities. One of the challenges still facing this SFF process

is the ability to accurately stop and restart the extrusion, which is necessary for the fabrication of geometrically complex parts.

2.2.4. SLA of Ceramics. The fabrication of ceramic parts using SLA technologies has also been investigated [13]. For this research, a standard SLA resin (Ciba XB5149) was used with silicone acrylate additions to retain SiO_2 during the binder burnout process. The SLA process was used to create green parts that are suitable for binder burnout. Reported densities average ~ 94% theoretical, however flexure strengths of green parts are very low (~ 170 MPa max). This is believed to be attributed to the delimitation of layers during the sintering process.

2.3. CURRENT INDUSTRIAL SYSTEMS

The technology to work with ceramics has been around for decades. Predominant methods for manufacturing ceramic parts involve the production of a mold negative in the shape of the desired part. Powdered ceramic is coated with small amounts of binder and then loaded into the mold. High pressure and heat are applied to create a green part in the shape of the mold. The green part is then sintered, usually in a low-pressure environment, to help increase the density and strength of the final part. Hot isostatic pressing or a similar process may be required for some ceramics to achieve maximum density.

The molding process is a tedious process that typically requires a large initial investment for every part alteration because new tooling has to be fabricated. This form of fabrication is typically restricted to simple shapes, and the ability to produce parts with holes is limited.

Another spin on this type of molding process is ceramic injection molding (CIM) [26]. This process specializes in small ceramic parts, and operates on a similar principle to that of plastic injection molding. Pressure and heat are applied to force binder-coated ceramic particles into complex molds. The abrasive nature of the ceramic powder causes wear on the metal components of the machines, and parts still require all of the green part processing of traditional ceramic molding to create parts of high density. CIM has advanced to the point of matching the results of plastic and metal injection molding processes within 30 μm of more than 10 different dimensional measurements.

Other techniques to create green parts include extrusion and slip casting. Tape casting, dry pressing, isostatic pressing, and hot pressing are also common techniques to create parts from ceramics. Conventional extrusion techniques require dies to be made for specific profiles and are limited in producible geometry, only allowing 2D profiles to be extruded. Slip casting typically produces weak green parts, and is more common for decorative and household ceramic items than industrial applications [32].

Tape-casting is capable of producing thin, flat ceramic parts with dried thicknesses ranging from sub-micron to millimeters. The popularity of tape casting gained momentum when its potential was realized for producing insulating substrates and multilayer capacitors for electronic parts. Tape-casting is now utilized for structural laminates, membranes, and solid oxide fuel cells but is limited to sheet type parts [34].

Pressing techniques to form ceramic parts are similar to those of the mold-based process mentioned above. The different forms of pressing each have their own advantages and disadvantages. However, due to the nature of the process, the geometric complexity achievable through these processes is basic when compared to the proven

versatility of traditional SLS processes. For simple shapes, a pressing method such as isostatic compaction could be examined to increase the final density of an SLS green part.

Machining is another common ceramic shaping process. Traditional machining operations of polishing, milling, drilling, and turning are possible on green ceramic blanks. Hi-speed machining with relatively slow feed rates, 12,000 rpm and 10 mm/s respectively, is more suitable for green parts [4]. Because the strength and hardness of many dense ceramics is so high, carbide or diamond tooling is often the only effective tooling for shaping ceramic blanks. The brittleness of ceramics makes chipping and sub-surface cracking difficult to avoid [16, 20]. Holes and small features are difficult to make consistently and accurately. A more preferred option for the creation of complex ceramic parts is net-shaped fabrication [4].

To make complex parts, such as a hydraulic turbine, machining and molding are currently the most practical options. Ceramic RP technologies have been able to produce ceramic parts of such complex geometries, but part mechanical properties have been less than those produced by molding techniques thus far.

The aim of this research is to create a rapid manufacturing process that will yield structural results similar to those achievable by common industrial ceramic fabrication techniques, while also offering the geometric capabilities of modern rapid prototyping processes. Utilizing the SLS process to make ceramic parts will dramatically decrease the amount of time it takes to go from a CAD model to a ceramic green part if successful. After that, traditional ceramic processing techniques may be applied to densify the ceramic part.

3. EXPERIMENTS

This section describes the equipment and processes used to accomplish the objectives of this research. The manufacturers and model numbers are given for equipment when available. The intent of this section is to enable the stated results to be reproduced given the proper equipment and procedure.

3.1. EXPERIMENTATION EQUIPMENT

This section describes the equipment and procedures used to collect and analyze the data for this research. Details of the SLS machine used to fabricate parts for this research are stated. Initial builds to understand and characterize specific features of this machine to produce high quality nylon parts are described. The SLS operating software is also discussed in this section.

3.1.1. Selective Laser Sintering Machine. A DTM Corporation (now merged into 3D Systems Corporation) Sinterstation 2000 was acquired from The Boeing Company and was first operational at UMR in January of 2006. A semester was spent working closely with Boeing partners and Integra Services International (Integra) associates to learn the capabilities and operating parameters of the machine and software. This older SLS system is preferable to a newer model for research purposes because it offered control flexibility to the user to adjust many operating features. Duraform™ (Nylon 12) was used during this time to understand the effects of build chamber and part profile parameters on part characteristics. Figure 3.1 shows a diagram of the machine setup. The maximum laser power and build chamber temperature is 50 W and 250°C, respectively. For a complete list of operating parameters, see Appendix A.

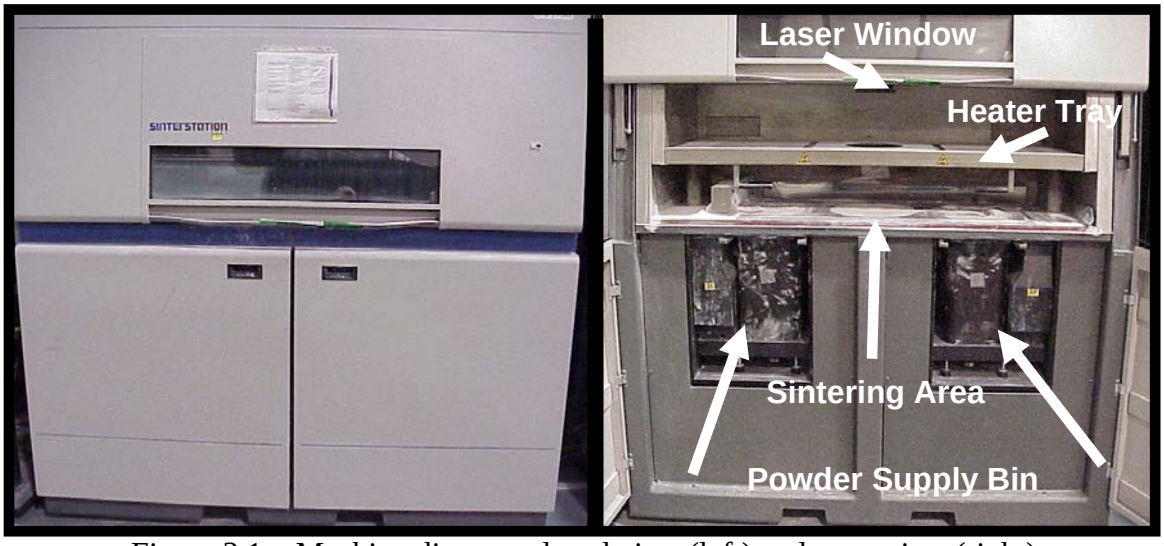

Figure 3.1: Machine diagram closed view (left) and open view (right)

Prior to conducting research on potentially new powders for the SLS process, the machine was calibrated by Integra. Several test builds were performed to find the proper scaling parameters to adjust STL files in order to produce accurate parts. One such scaling test build was performed using 69 numbered parts spaced evenly over the build area as shown in Figure 3.2. The numbered bottom of an individual scale piece is shown as (a) in Figure 3.2; (b) shows the arrangement of all of the scale pieces; (c) shows all of the labeled design features of an individual scale piece. The results of the study identified the preferred build locations of the for quality parts. This will be specific to individual SLS machines because if cool spot variations and laser window characteristics (scratch and other imperfections).

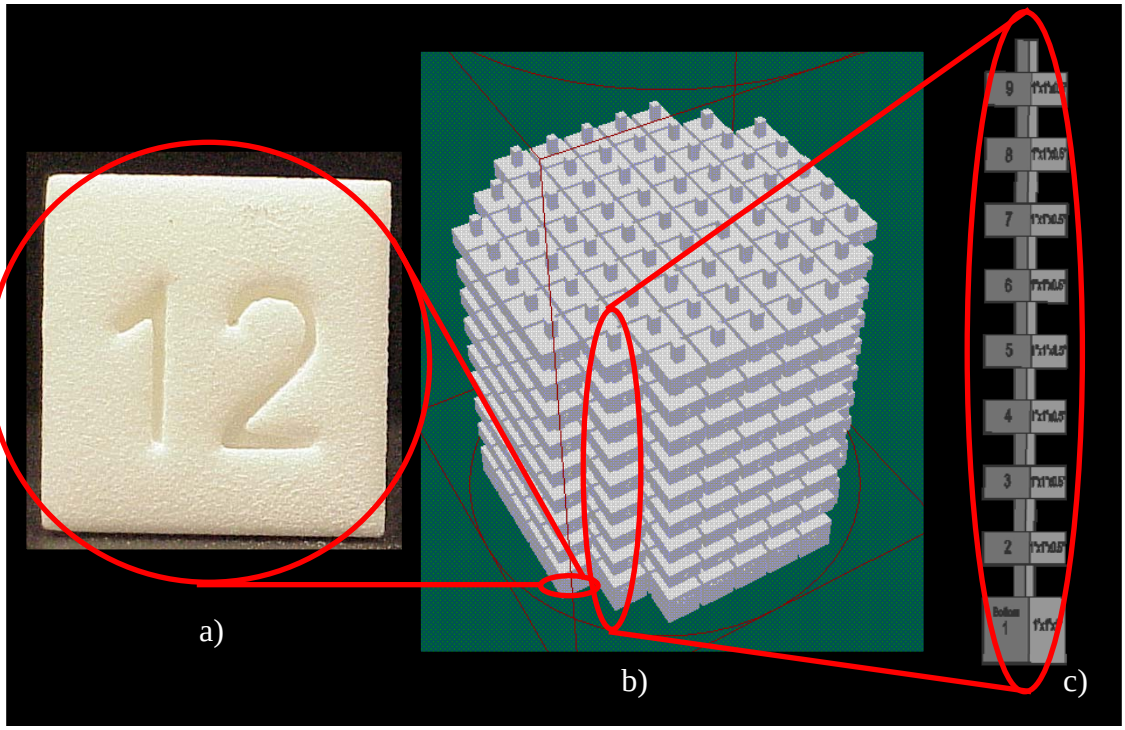

Figure 3.2: View of nylon scale piece (a) bottom (b) build layout (c) CAD model

3.1.2. Basic Part Build Parameter Studies. Several thick and thin walled parts of various geometries were produced to study the effects of part placement (part location in the build area), part orientation (the orientation of the part in relation to the X, Y, and Z axis), and sacrificial part layout. A sacrificial part is one built in the vicinity of the desired part to better stabilize the powder temperature immediately surrounding the desired part. An example of this is shown in Figure 3.3. The "heat fence", which consists of several tensile test bars lined up at the bottom of the build, provides a more uniform thermal base for parts to be built above. Curling is often seen in the initial layers of the heat fence, but not in the parts above provided that the proper build parameters are set. A 0.1 in gap between the heat fence and the desired parts above it is sufficient to prevent the heat fence from fusing together with the other parts, but provide local thermal

stabilization for the build. The pictured heat fence only contains 5 bars, each roughly 6.5x0.75x0.125 in. Additional bars may be added of different sizes to provide adequate coverage for builds with a larger footprint than covered by this heat fence.

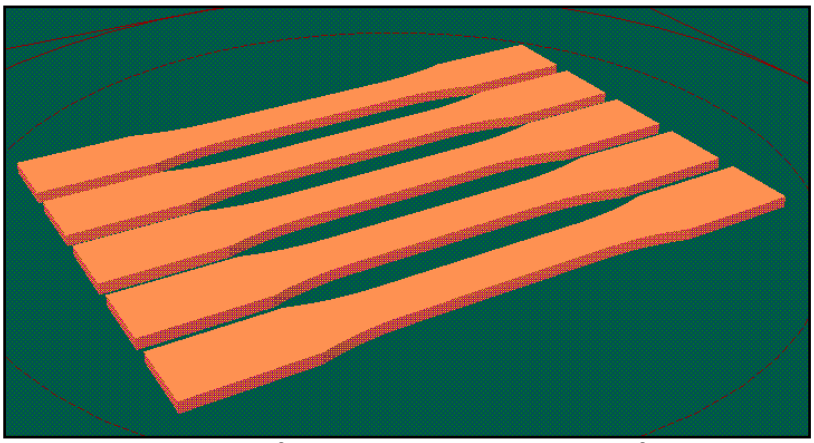

Figure 3.3: Heat fence placed at the bottom of the build

In addition to a heat fence, thin blocks ranging from 0.125 to 0.25 inches in thickness or smaller tensile test coupons are placed around thin sections of parts. The main benefit of including such sacrificial parts in a build is that part curl is reduced. Curling can be compensated for in several ways (increasing the temperature in the build area and feed powder bin area, adjusting laser parameters, etc.), but doing so does not always fully eliminate the curling issue. Figure 3.4 shows the difference between a portion of a plane wing that was made with sacrificial parts surrounding it and another without. Figure 3.5 shows an example of a sacrificial part layout to help produce good quality wings on an airplane.

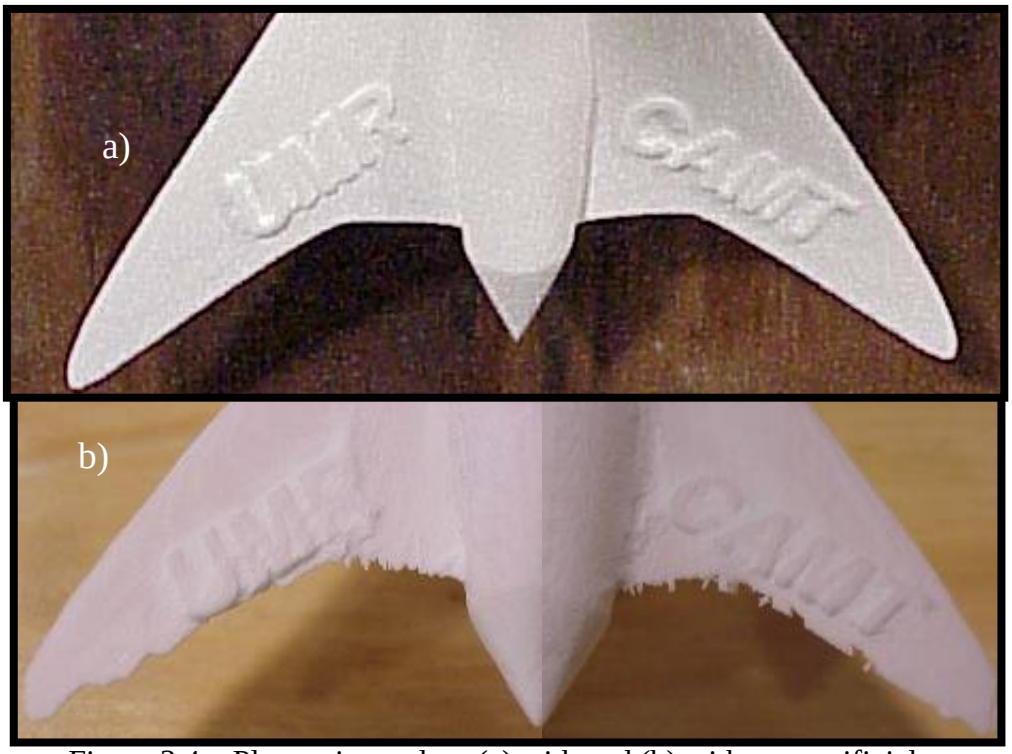

Figure 3.4: Plane wings edges (a) with and (b) without sacrificial parts

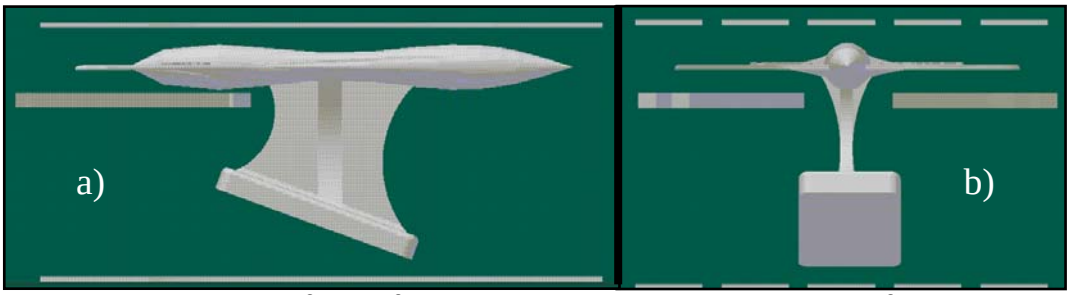

Figure 3.5: Aircraft sacrificial part layout (a) side view and (b) front view

3.1.3. SLS Operating Software. The operating software for the Sinterstation 2000 used in this research is version 2.1. The software provides several useful features for part manipulation. Each part in a build is imported as an STL file, which is a typical

form of machine part file that is easily sliced into layers and converted into machine code. The software allows for easy part relocation, rotation, and scaling once the STL file is imported. Laser operating parameters and build parameters are set for each part. A material must be assigned to the build in the software, which establishes a range of operating parameters for the build. If a specified parameter is outside of the suggested range for the specified material, a warning is registered, but can be overridden. The ability to override a warning is useful for experimenting with parameters outside of the predefined range.

The software also allows for manual control of machine operations. This proves to be invaluable for testing heater output, laser power, and build area heating. The powder bins, part build area piston, and powder roller are a few of the features that can be controlled in manual mode. These functions are useful for cleaning, performing maintenance, part removal, and build chamber preparation.

Other useful features of the software package include a preview function that shows a slice-by-slice view of the build file and collision detection. These are useful for checking to see if parts will intersect one another as they are arranged in the build prior to the actual job starting. Another handy feature is that once the build has started, parameters can still be adjusted for the layers and parts above the layer currently being built. Parts can even be added or subtracted to and from the build while the machine is operating.

3.2. EXPERIMENTAL POWDER PREPARATION

Alumina (Al_2O_3) was chosen as the high-temperature ceramic for this research project due to its availability and economical feasibility ($6.35/kg). The powder has a purity of 99.8% Al_2O_3, surface area of 8.9 m^2/g, and an average particle size of 0.4 μm [27]. As mentioned above, the small particle size is an important characteristic for producing final ceramic parts of relatively high flexural strength and density. For example, it has been shown that an increase in particle size from 1.4 to 4.8 μm of alumina results in an increase in sintering temperature from 1500 to 1675˚C and that the strength of the final part decreases [11]. Several different binders and preparation methods were used in this project.

3.2.1. Binder Experimentation. Thermoplastics are common to the SLS process and are a popular choice for binders in SLS of ceramic powders [6, 8]. Because of such, PMMA (Polymethyl-methacrylate) was chosen as the first trial binder. PMMA was initially dry-mixed in a ball-mill, but, regardless of the volume fraction of the binder, no successful green parts were produced in the SLS machine. PMMA was then dissolved in Tetrahydrofuran over a 24-hour period with constant stirring. Again, varying amounts of alumina were added to create several mixtures of different PMMA to alumina percent volume fraction powders. The mixtures were dried and then crushed in a blender. The particle size was further reduced by 4 hours of ball milling. To ensure that the particles were of a size similar to that of the Duraform™, the powder was meticulously sieved through several layers of decreasing screen size.

Several attempts were made to produce green parts with the SLS machine using several different operating parameters, but none of the SLS parameter adjustments

produced successful parts. New mixing methods and several different PMMA/alumina combinations were tried. Each produced the same result – no viable green part that could withstand the binder burnout process.

Investigation into new binder possibilities began. The results of the investigation led to experimentation with stearic acid ($CH_3(CH_2)_{16}COOH$). The binder has a relatively low melting point, approximately 69°C, is rather inexpensive ($15.10/kg), and has a hydroxyl group to help the particles bond with the alumina. Hydroxyl groups are known to help organic binders bond to oxide ceramics like alumina (Al_2O_3) [3, 8].

Dry mixing has been shown as a viable means to create suitable binder-coated ceramic powder for SLS [3]. Mixtures ranging from 40 to 50 vol % stearic acid were prepared by ball-milling the two powders in a standard tumbler. Parts were successfully made using the 50 vol % stearic acid powder, and they had enough green strength to not be damaged during careful part break out and transport. No successful green parts were created using the 40 vol % stearic acid powder. Sieving the powder with a 35-mesh screen isolated the desired particle size. The 50 vol % stearic acid powder was used to produce the results stated in this thesis.

3.2.2. Composite Powder Characterization and Understanding. To better understand the characteristics of the composite powder, a thermogravimetric analysis (TGA) was conducted (Shimadzu model TGA-50) in air with a heating rate of 10 °C/min. The TGA result shown in Figure 3.6 indicates that binder removal begins at 150°C and is completely removed at approximately 400°C. This information was useful in determining an appropriate binder burnout temperature profile. Particle size and

distribution of the alumina powder was measured using a Beckman Coulter laser scattering particle analyzer (model LS 13320).

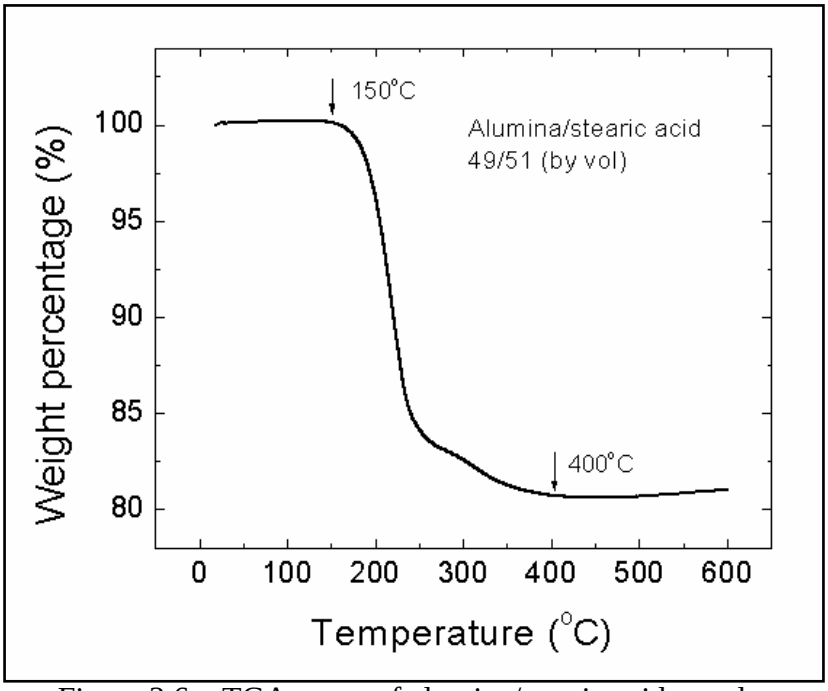

Figure 3.6: TGA curve of alumina/stearic acid powder

3.3. MEASUREMENTS AND ANALYSIS

Property measurements involved the analysis and documentation of both mechanical properties, such as flexural strength and surface roughness, and physical characteristics like density and grain size. This section describes the specific equipment and processes used to collect such information about part and process details.

3.3.1. Density Measurements. Dry density values of green parts were determined by measuring the volumetric dimensions and weight of test bars that were designed with double the dimensions of an ASTM C1161 standard b-bar. Mitutoyo Absolute Digimatic digital calipers (Model No. CD-6”CS, Serial No. 03377881) with a resolution of ±0.01 mm were used to measure the height, width, and length of the bars. A digital gram scale (Acculab Vicon SN 19054727) with a resolution of ±1 g was used to measure the weight of the green bars. Multiple measurements of the same parts were conducted to validate the results.

The densities of fully sintered bars and binder burnout bars were measured using the Archimedes method. Again, multiple measurements of parts were taken to validate the results. A total of 3 flexural strength bars were measured for the maximum density. The scale used for these measurements was a DeltaRange AG204, and has a resolution of ±0.0001 g.

3.3.2. Flexural Strength. Flexural strength was measured using an Instron 4-point bending test machine (model 5881). Fully sintered bars were polished in accordance to with the standard procedure specified by ASTM C1161. The samples were ground to b-bar regulations (45x4x3 mm^3) with the rounded corners, and final polishing was performed by a 600 grit diamond wheel. A total of 4 flexural strength test bars were measured.

3.3.3. Fracture Surface Images. The scanning electron microscope (SEM) images were taken with a Jeol 330. Low and high magnifications were used to study the microstructure of sintered flexural strength test bars and ones after completing the binder burnout cycle.

3.3.4. Surface Roughness Analyzer. Surface roughness measurements were taken using a Mitutoyo SJ-201P. Flexural strength test bars were measured at twelve different locations and then averaged to produce the average surface roughness measurement for a single bar. The results of 8 bars were averaged to produce the overall average surface roughness measurement for the process.

3.4. MACHINE EXPERIMENTATION

The flexibility of the DTM Sinterstation 2000 is ideal for experimenting with new powders and processes for SLS. The ability to create build profiles with parameters outside of the preset operating parameters for a standard SLS material is essential to this research. The material properties of the stearic acid/alumina powder limited the SLS machine to the narrow range of various parameters that are listed in Appendix A.

3.4.1. Machine Material Setting. For every experimental build, the SLS machine material setting was set as Duraform™. Build chamber temperatures varied from 58 to 63°C and the laser power ranged from 3.3 to 6.2 Watts. No greater laser power was used because the area being fused by the laser smoked when scanned with laser powers greater than 6.2 Watts due to binder break down. The machine's maximum capabilities for a build chamber temperature and laser power are 250°C and 50 Watts.

3.4.2. Machine Modifications. A new center heater and heat deflector system was installed part way through the research. The new heater is a square, dual core heater from Integra and brings the build area to temperature more quickly (~23 °C/min for the new heater versus ~27 °C/min for the old) than the old round heater that came standard on the machine. The new heat deflector was a necessity to accommodate the shape of the

new heater. Figure 3.7 shows a thermal image of the new heater versus the old, round heater. Notice that the new heater has a uniform core temperature (all white) and the old heater has cool spots (darker areas). The dark areas in the middle are where the laser shines through. The different shapes of the heaters warranted a remapping of the cool spots in the build chamber. The quicker response time of the new heater helped to reduce the significance of these areas but part location studies proved valuable for part placement of test parts.

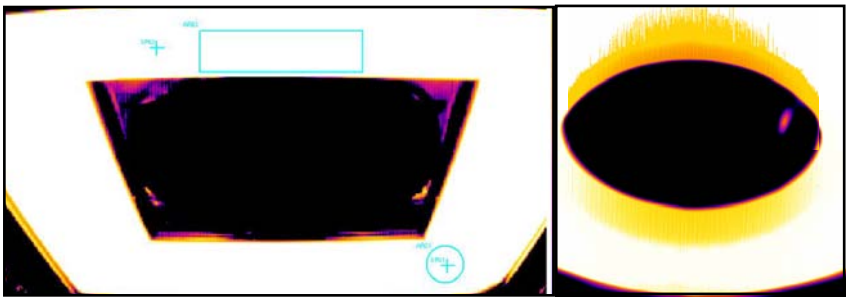

Figure 3.7: Thermal images of new (left) and old center heater (right)

New heat deflectors were made in house to accommodate the new heater's shape. The hinged deflectors allow for a swing angle of ±90 degrees (as indicated by the red arrows in Figure 3.8). The hinge feature is necessary to allow the roller to pass over the build area. The hinged deflectors allow for a sharper temperature gradient between the feed powder bins and the build area. The new heat deflectors allowed for no heat saturation in the powder bin areas after the center-upper part heater was set at 70°C for 5 minutes. The old heater allowed for ~2°C saturation of the power bin area under the

same test conditions. Effective temperature gradients are important for working with the experimental powders used in this research to ensure that a clean, smooth layer of powder is spread across the laser scanning area. The idea for the hinged deflectors came after viewing the heat deflectors of other, more modern SLS machines. No modification had to be made to the Sinterstation 2000 for the new deflectors to be installed or to operate.

A new laser window was purchased from Integra to replace the scratched laser window that came with the machine. The laser was recalibrated for the new window. Figure 3.9 plots the measured laser power versus the laser power input from the machine.

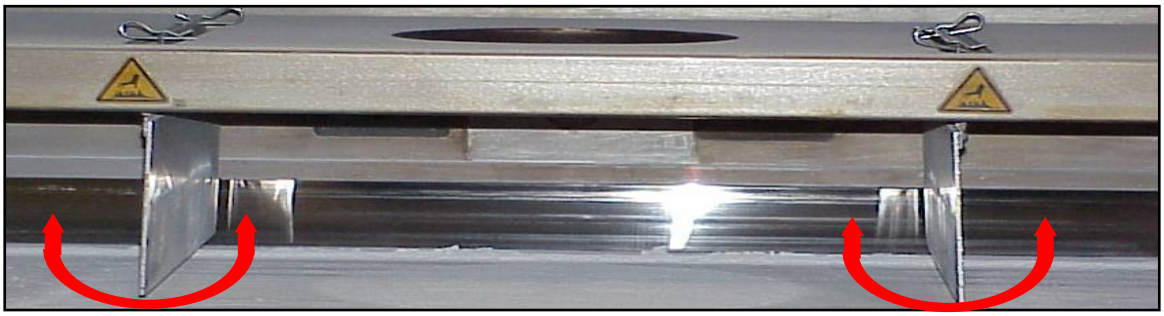

Figure 3.8: Hinged heat deflectors that allow ±90 degree rotation

The laser power measurements were taken with an Ophir power receiver (SN 145602) and Nove 2 laser power meter with a resolution of ±0.1 Watts. All values presented in this thesis are the corrected laser power values. A line of best fit was used to interpolate any laser value that was not directly measured during the laser power verification. For example, to get a value of 20 W to strike the build area, an input laser powder of 23 W would be programmed (with the new laser lens installed).

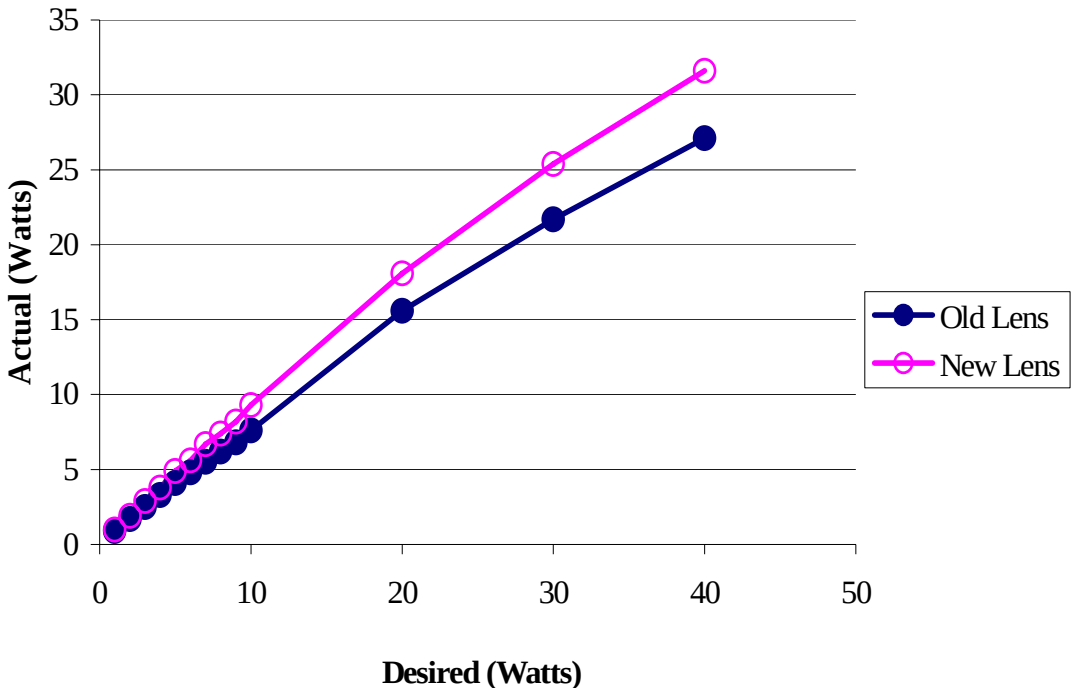

Figure 3.9: Laser power measurements vs. input

3.4.3. Part Breakout Process. The removal of parts from the SLS machine involves raising the part cylinder and sliding out the powder column after a build is completed. The powder column consists of the fused green parts buried in the surrounding loose powder. This is carried on a tray to the break out station where exhaust fans and vacuums help to manage the dust generated by the breakout process. The loose exterior powder is delicately removed by hand, rubber brush, scraper, or compressed air. A scraper was used to remove the powder far from the green parts and pressurized air (set at approximately 10 psi) was used to reveal the green parts. Once removed from the part cake, the green parts were blasted with 20 psi of air to remove the loosely bonded powder surrounding the part. For parts with holes, pressures up to 30 psi

were used to remove excess powder from the holes. Caution had to be used to prevent damage to the green parts when using pressures exceeding 15 psi.

3.5. BINDER BURNOUT PROCESS AND FINAL SINTERING

The binder burnout process was carried out in air in a Fisher Science Isotemp muffle furnace, model 550-126. Traditional ceramic processing suggests that an ideal binder burnout temperature profile should be a slow, consistent temperature increase, one that has a curve similar to that of Program 1 shown in Figure 3.10. For Program 1 the temperature was increased from room temperature to 600˚C at a rate of 0.2 ˚C/min, dwelled at 600˚C for 120 min, and then cooled at rate of 10 ˚C/min to room temperature. In addition to this profile, a temperature profile with variable rate of increase was also tried – Program 2 of Figure 3.10. The steps in Program 2 are listed in order in Table 3.1.

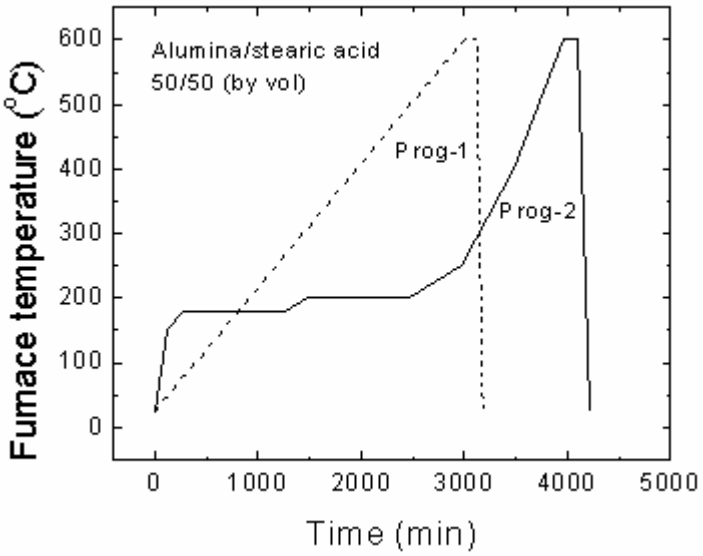

Figure 3.10: Two temperature profiles used for binder burnout

Table 3.1: Program 2 temperature profile heating rates

Time to Temp (min)	Heating Rate (°C/min)	Final Temp of Stage (°C)
120	1.000	120
2000	0.030	180
1500	0.047	250
600	0.250	400
200	1.000	600
120	0.000	600
200	-2.875	25

Program 2 was designed to ramp quickly (1.0 °C/min) to the temperature where the stearic acid begins to break down, and then slowly increase the temperature (0.03 and 0.047 °C/min) through the temperature range where the stearic acid most rapidly leaves the part. This makes for a less volatile binder burnout, which helps to minimize surface cracking by breaking down the binder at slower, more controlled rate. The program then quickly increases temperature to the maximum temperature (600°C) of the cycle to breakdown any remaining binder. Dwelling at this temperature ensures that all of the binder has been removed from the green parts. After cooling, the parts retain enough strength for safe transport to the sintering furnace, but are still fragile.

The final sintering was performed at 1,600˚C. Heating occurred at 5 °C/min until 1,600˚C was reached. That temperature was maintained for 2 hours in a Lindberg furnace (model 51644) and then the part was cooled at a rate 10 ˚C\min.

4. RESULTS AND DISCUSSION

4.1. EXPERIMENTAL SLS POWDERS

Two different binders were tried in this research. The first was PMMA, which has produced several successful green parts in other research projects. The second, stearic acid, had several characteristics to suggest it had the potential to be a good binder for the alumina ceramic.

4.1.1. PMMA Experimentation. In other documented research projects, PMMA has been shown to be a suitable binder for coating ceramic powders [17]. Small green parts made by SLS from such powders exhibit sufficient strength to be handled without damage. Initial powder preparation techniques and SLS process parameters for this project were chosen based on previous work. However, no successful fully sintered parts were produced.

The primary operating parameters varied in this study were part, feed, and piston heater temperatures; laser power, scan spacing, speed, and count; and feed rate and layer thickness. Appendix B shows the various combinations of parameters attempted to create successful green parts with the PMMA/alumina powder in the SLS machine.

Initially, the powder did not spread well in the SLS build chamber because the particles clumped together as the roller pushed them. The roller pushed the clumps along the top of the powder layer. If a clump hit an area that had just been fused, it would either roll up a part if it were a few layers thick, move a part to a different location in the build chamber, or unevenly press parts into the part cake. The only way that a build could recover from this problem was to decrease the feed powder temperatures and let the

build continue (the specific parts were deformed beyond repair) or bury the build using manual program functions and start over. No SLS solution was found for this problem.

In an attempt to improve the flow of powder in the SLS process, different concentrations of mineral oil were added to act as a lubricant during the spreading of the powder. Initially 50 g of mineral oil was mixed with 50 ml of THF. The rest of the process for producing the powder was the same. The mineral oil also worked as a catalyst for the fusing process, acting as a plasticizer for the PMMA. Table 4.1 shows how the increase in mass ratio of mineral oil to that of PMMA lowered the fusing temperature of the powder. It also shows the mass yield percent, which is the mass of powder after sieving divided by the mass of the powder before sieving. The results show that the mineral oil causes the powder to retain larger clumps after ball milling. This fact increased the powder preparation time by approximately a day.

Table 4.1: Effect of mineral oil on PMMA powder

Mass ratio of mineral oil to PMMA	0	0.1	0.2
Mass yield, %	52	43	38
Temperature of gluing, ^{o}C	250	220	195

The results of further experiments with this powder were unsuccessful. However, knowledge about the characteristics of a binder-coated alumina powder improved the future development of experimental powders.

Experimentation with the SLS of the PMMA powder produced sparks when the laser struck the powder in the build chamber. The sparks were believed to be from the laser directly hitting alumina particles and not the binder. Large amounts of smoke also rose from the build area if the temperature of the powder bed got too high, whether it be from laser scanning or chamber heating. The mineral oil is believed to be the substance causing the smoking. Figure 4.1 shows an example of an experimental build where the laser power was varied over a bed of PMMA-coated alumina. The discoloration of the bars in Figure 4.1 was caused by the charring of the powder. The light grey bar (1) at the top of the picture was an indicator that process parameters were approaching more favorable conditions for producing green parts by not breaking down as much of the binder as in the other two bars. Bars 2 and 3 were charred from too intense of laser power burning the binder.

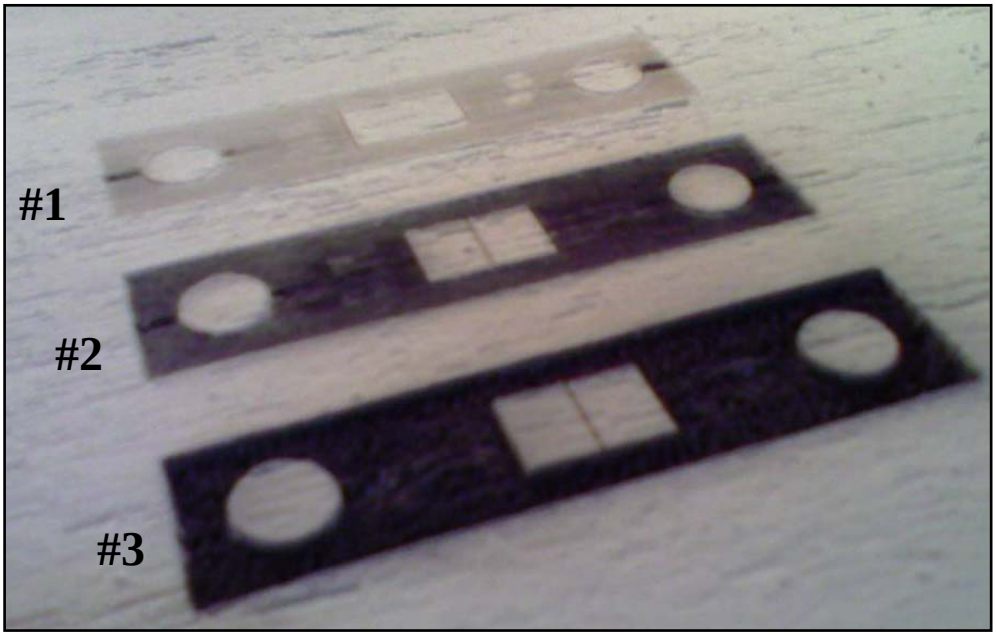

Figure 4.1: Mineral oil/PMMA/alumina powder in the SLS chamber

Green parts were eventually produced using the mineral oil/PMMA/alumina blend of powder. The parts could be broken out of the build, but would collapse under their own weight when handled. Figure 4.2 shows an example of the best results from experimentation using PMMA as a binder in this research. The disappointments of the many failed attempts were motivation to explore a new direction in binder materials.

Figure 4.2: The best results achieved in this research using PMMA as a binder

4.1.2. Initial Stearic Acid Experimentation. The use of stearic acid has several benefits over that of PMMA. After several failed attempts to work with PMMA, stearic acid presented itself as a much more attractive option. Initial SLS operating parameter assignments were based on known material properties with similar binders [17]. The 50 vol % stearic acid to alumina ratio was selected as a starting point based on the success of other projects working with that ratio even though different binders were used.

The experimentation with PMMA powder and mineral oil/PMMA mix provided experience and insight into what were some of the key characteristics of an SLS friendly powder. For instance, the powder had to resemble the particle size of the Duraform™ (≤

90 μm) to create a smooth powder bed for fusing. There needed to be a significant temperature difference (≥ 75°C) between the binder melting point and the temperature of the feed powder to prevent clumping of the powder; the PMMA powder was eventually lowered to a temperature 10°C above room temperature. More attention had to be given to the packing of powder in the feed bins than was given for the Duraform™ to ensure that the roller would effectively spread a complete layer of fresh powder over the build area instead of just packing the powder down and not spreading any at all, or short feeding.

Successful green bars were produced using the operating parameters listed in Table 4.2. The build chamber was used to bring the experimental powder near the melting point of the binder (69°C). The laser supplied the remainder of the energy needed for fusing the binder particles. Because of the relatively low build chamber temperature (62.5°C for the stearic acid compared to that of the ~180˚C used for Nylon 12) being so close to the binder melting point, three low-level laser power settings were used to supply the remaining energy needed to create green parts. To better ensure that the laser energy was adequately applied to the parts, a laser scan count of 2 was used (meaning that the laser scans the same path twice), and the scan speed was reduced from the typical 49.5 in/sec for Nylon 12 to 35 in/sec.

These bars underwent a binder burnout process using Prog-1 discussed in Section 3.5 of this thesis. Figure 4.3 shows the stearic acid/alumina green bars and the fully sintered bars of pure alumina. The sintered bars had low relative densities that ranged from approximately 78% to 81%. The bars are ordered from lowest to highest laser power in Figure 4.3. Note the significant difference in size between the three; the 4.1 W

bar is approximately 9% larger than the 3.3 W, and the 4.8 W is approximately 9% larger than the 4.1 W bar as well. The design called for each bar to be the same size. The bars were cracked and broken during the binder burnout process.

Table 4.2: Initial operating parameters for successful stearic acid green part

Parameter	Value
Build Chamber Temp	60°C
Laser Power	3.3, 4.1, and 4.8 Watts
Laser Scan Count	2
Laser Scan Speed	35 in/sec
Laser Scan Spacing	0.005 in

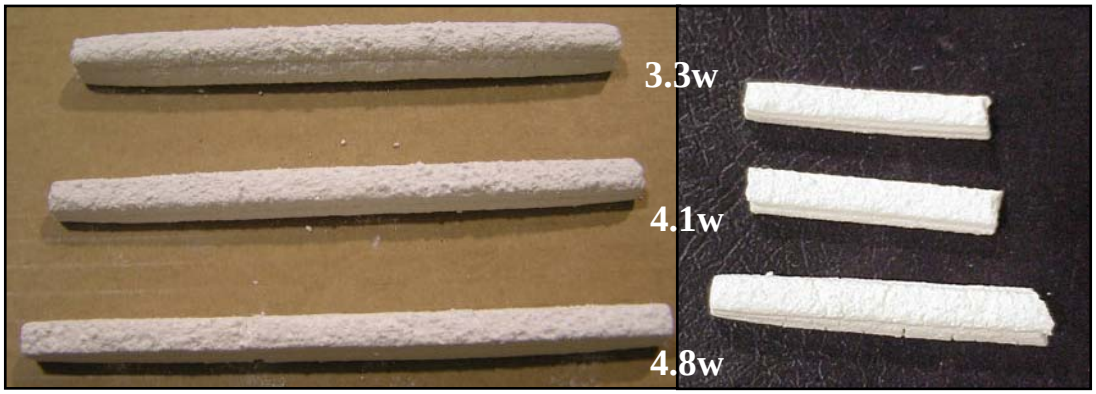

Figure 4.3: First stearic acid/alumina green parts produced by SLS and sintered

4.2. SLS PROCESS REFINEMENT

Following the production of the first stearic acid-alumina green parts, investigation began to find the optimum SLS operating parameters to create sintered parts

with the highest density and flexural strength possible. The primary parameters adjusted were laser power, build area temperature, and the laser scanning characteristics. The following sections discuss the challenges and how they were overcome.

4.2.1. Surface Cracking and Bottom Bulging. Eliminating the cracks on the surface of the parts is a requirement for any part or process to be viable in industry. Figure 4.4 shows a common example of severe surface cracking in early flexural test bars.

Figure 4.4: Example of severe surface cracking of green part

Bulging was a deformation found at the bottom of all green parts. The trend was that the larger the initial surface exposure to the cooler, non-fused powder, the larger the bulging effect. Figure 4.5 shows an example of said bulging at the top of the photograph. In the picture, the bar is upside-down. The top of the pictured part was the bottom of the part in the build and was the first profile scanned of the part.

Two predominant theories existed that suggest this effect was caused by either excess laser energy penetrating beyond the desired build layer or by curling of the part shortly following the fusing of the initial layers. The shape of the bulging supported both theories; the center of the bottom face always protruded farther down than the edges. This suggested that edges curled up or that there was greater thermal penetration in the

middle of the part. To better understand this issue, the effects of adjusting single process parameters were studied.

Figure 4.5: Photo of bulging effect

The fact that the bulging only occurs on the bottom of parts suggests that laser energy penetrates well beyond the specified layer thickness (0.13 mm). If curling were the issue, one might expect to see a relatively uniform deformation (curling of the entire part) in parts such as flexural strength test bars and other parts with a rectangular cross-section. The predominant deformation of green parts in this case is only on the bottom of the part. Top surfaces and sides of bars are flat and the corners are sharp. The parts also show no visible curl when the build is observed. For these reasons, the suspicion of excess laser energy penetration was first investigated.

The theory of excess laser energy penetration was supported by the direct correlation of increased bulging with increased laser power. The idea was that after the laser energy fused the first layer of a profile, the heat began to dissipate into the surrounding cooler powder. Another layer of cool powder began to bond to the fused

profile and was then scanned again by the laser, the heating affects of which penetrated beyond a single layer thickness. As this process repeated, heat was stored in the fused areas. Therefore, the thicker the cross-section of the part, the more heat it stored from the SLS process. Bulging was greater for thicker parts because the larger amount of heat stored in the part from the process mentioned above created a larger heat-affected zone. Thinner parts had a smaller heat-affected zone that dissipated heat faster, thus creating a smaller heat-affected zone. The center of the profile also retained more heat than the outer sections and fused with more of the powder below the first layer than the edges did because they had dissipated more heat for a given amount of time. This process is additive for each layer until the laser energy penetration (heat) no longer extended beyond the depth of part. That would account for why the tops of parts and sides did not show signs of curl. The full understanding of this affect was beyond the scope of this thesis study.

To begin to understand and correct for this defect, the laser scan count was decreased from 2 to 1. Significant improvements to green parts were seen immediately. The bulging decreased and macroscopic surface cracking was minimized. Figure 4.6 shows examples of three different bars created at different locations in the build area using different laser powers. The bulging effect was an example of the importance of identifying and understanding proper energy delivery to the part fusing area. The refined SLS process parameters are shown in Table 4.3.

With these SLS parameter settings, the most promising results to-date were achieved to provide the density and flexural strength mentioned in the abstract. Thus far, only 4 bars have been measured and verified for flexural strength. They were tested as

described in the experimentation section. Table 4.4 shows the individual bar's flexural strength results, and Table 4.5 shows the average density measurements thus far for different laser powers. The relative density is based on the theoretical density of a pure alumina part being 3.96 g/cm^3. Note that the flexural strength of an 85% alumina vitreous body ranges from 205 to 310 MPa [29]. An average flexural strength of a 99.9% alumina part is approximately 400 MPa [30].

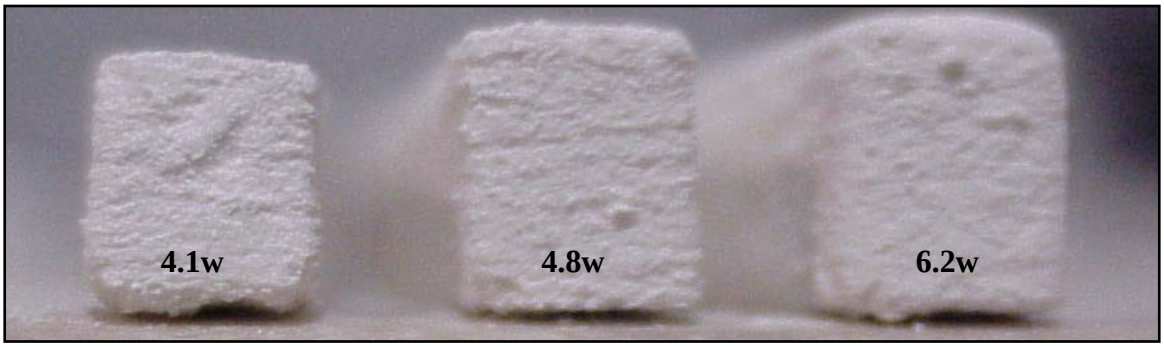

Figure 4.6: Bars fused at 4.1, 4.8, and 6.2 watts with scan count of 1

Table 4.3: Shows the refined range of major build parameters for stearic acid parts

Parameter	Value
Build	62°C
Laser Power	4.1,4.8, and 6.2 Watts
Laser Scan Count	1
Laser Scan Speed	35 in/sec
Laser Scan Spacing	0.005 in

Table 4.4: Bar flexural strength

Samples	Flexural Strength (MPa)
Sample 1	232
Sample 2	261
Sample 3	279
Sample 4	246

Table 4.5: Average part density for different laser powers

Sample	Laser Power (Watts)	Density (g/cm^3)	Re. Density (%)
Alumina	3.2	3.38	85.3
Alumina	4.1	3.44	86.9
Alumina	4.8	3.50	88.4

4.2.2. Energy Density. A common equation used to describe the energy density applied by the laser to the surface of a fused area is shown below as Equation 1 [6]. In the equation, *P* is power, *BS* is laser beam spacing, and *SCSP* is the scan speed of the laser.

$$Energy\_Density(kJ/m^2) = \frac{P}{BS * SCSP} \quad (1)$$

Using the above equation and the discussed experimental results, an energy density of approximately 42.5kJ/m^2 proved to be the most effective compromise between geometric accuracy and green density. Finding this value was the result of several

experiments to examine effects of individual parameters. Laser powers ranging from 4.1 Watts to 6.2 Watts were used to properly gage the effects of individual build characteristics.

4.3. PART GEOMETRIC INACCURACY

A common interest of most ceramic processing studies, regardless of the fabrication technique, is part shrinkage during burnout and sintering. Understanding this fundamental characteristic of ceramic manufacturing is essential to produce industrially accepted parts. Gathering enough knowledge to accurately account for the geometric enlargements that occur during the creation of the green part and for the shrinkages that occur during binder burnout and final sintering is a crucial requirement for this project.

4.3.1. Green Part Inaccuracy. Batches of flexural test bars were built in layers of 12. Figure 4.7 shows an example of one layer of a batch of flexural test bars, and Figure 4.8 shows how the parts were oriented inside the SLS build chamber. Part orientation and location are key elements in this study, and will be discussed later. The data sets for the shrinkage were gathered by taking multiple measurements, at least twice in a random order for verification, in all three dimensions of the flexural strength test bars (length, width, and height). In Figure 4.8, the numbers are placed on the bars for organizational purposes. For a point of reference, the designed dimensions of the flexural strength bars are 90 mm long, 6 mm wide, and 8 mm tall.

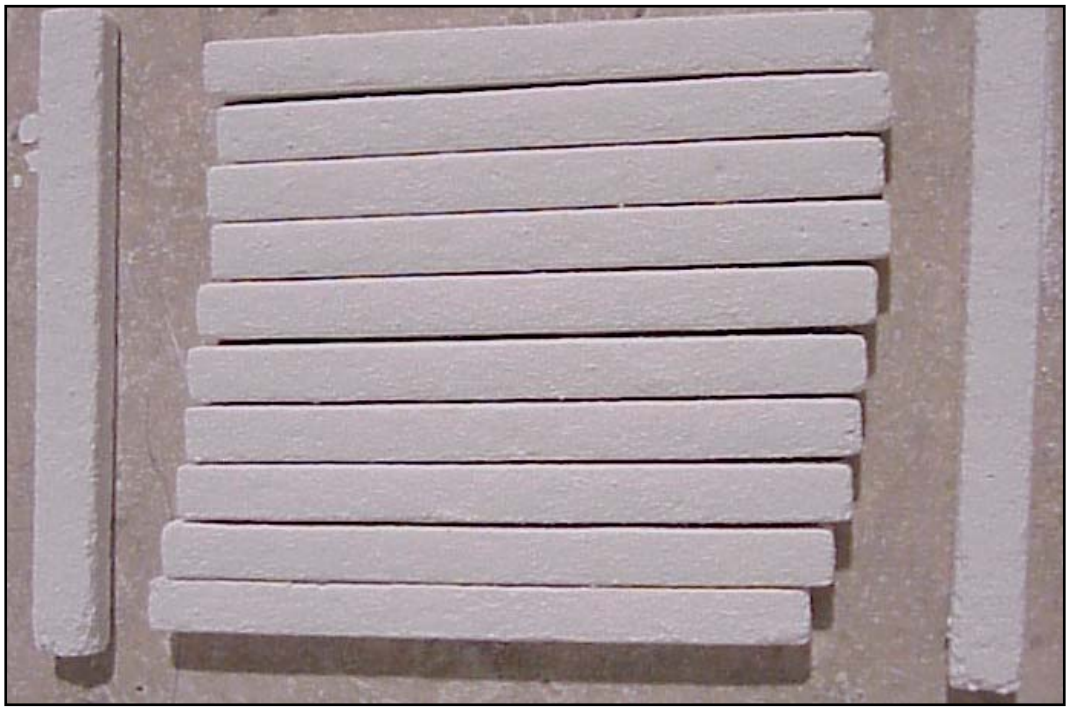

Figure 4.7: Batch of green flexural test bars

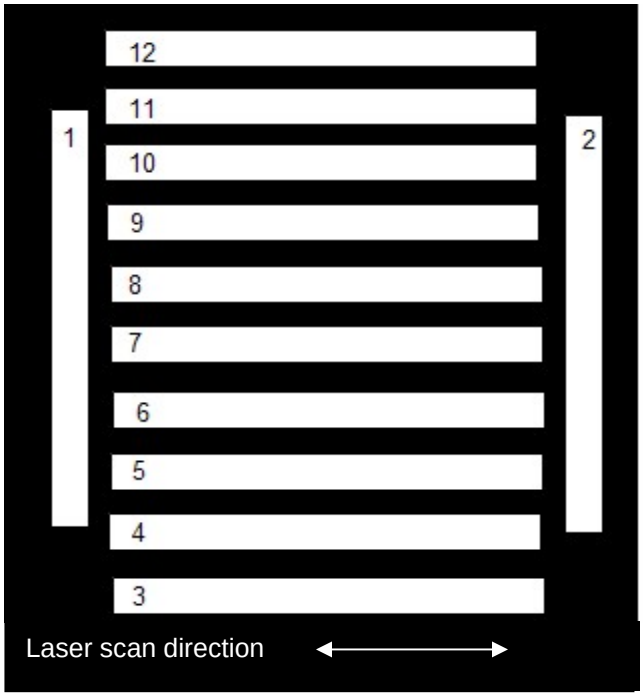

Figure 4.8: Fracture test bar build layout

Table 4.6 shows the average difference between the designed and actual dimensions of green flexure test bars. The least amount of deviation from designed dimensions occurred with a laser power of 4.1 W, the lowest of the three laser powers. The amount of part deformation increased with increased laser power for the green parts. This supported the theory that the swelling and bulging are a result of the heat affected zone created from excess of the fusion process bonding surrounding powdered to the scanned part profile.

Table 4.6: Initial average variations from part design values

Laser P (W)	Length (mm)	% Diff	Width (mm)	% Diff	Height (mm)	% Diff
4.1	93.17	3.5	8.91	48.5	10.20	27.5
4.8	93.95	4.4	10.09	68.1	10.63	32.9
6.2	95.14	5.7	12.14	102.3	11.79	47.3

These values were brought closer to the designed dimensions with further process parameter adjustments. The significant improvements were attributed to a reduction in laser scan count from 2 to 1. This effectively cut the applied laser energy in half. Minor improvements were made to better the part accuracy by working with both laser parameters and part orientation. Table 4.7 shows the averaged results for the revised operation parameters. On average, the length, width, and height of a bar decreased by 0.68 mm (0.8%), 1.98 mm (33.1%), and 0.67 mm (8.3%) respectively, from the results in Table 4.6. These numbers represent the average differences between the averaged bar dimensions listed in Tables 4.6 and 4.7.

Table 4.7: Average dimensional green part variation from SLS after initial adjustments

Laser P (W)	Length (mm)	% Diff	Width (mm)	% Diff	Height (mm)	% Diff
4.1	92.75	3.1	7.60	26.6	9.51	18.9
4.8	93.32	3.7	8.02	33.7	10.00	25.1
6.2	94.14	4.6	9.57	59.5	11.11	38.9

After final sintering, the bars show significant deviation from the green parts. Table 4.8 shows the difference between the sintered and the green part dimensions. All of the data used to calculate these figures is available in Appendix C. The shrinkage was partly due to the porosity of the green parts (roughly 50%) and the removal of binder (50/50 %vol. stearic acid/alumina). The largest average relative shrinkage for bars was in the z-orientation of the build (the height of the part). The average of the relative shrinkages in each dimension of the bar were 16.4%, 23.6%, and 25.1% for the respective height, width, and length.

Table 4.8: Overall shrinkage of part

	Length		Width		Height	
LP (Watts)	(mm)	%Diff	(mm)	%Diff	(mm)	%Diff
4.1	14.85	16.0	1.65	21.7	2.30	24.2
4.8	15.17	16.3	1.55	19.3	2.30	23.0
6.2	16.05	17.0	2.84	29.7	3.11	28.0

The results of this study suggested that a laser power of roughly 4.8 Watts was the best for producing geometrically and dimensionally accurate parts because the least amount of relative shrinkage occurred during the sintering of parts made from this laser power. The associated powder bed energy density is approximately 42.5 kJ/m^2. The supposition was that the least amount of shrinkage between green and dense parts maximize the likelihood of parts completing binder burnout and sintering with minimal distortion. The reasons why this energy density resulted in the least amount of shrinkage between the three different power settings were unknown. The complete understanding of this observation goes beyond the scope of this thesis.

Minimal shrinkage during the sintering process was desired to achieve the best results during binder burnout and sintering. This was most easily seen in the sintering of complex geometries that have sharp variations in part thickness such as at the joint of the plane wings and body. If the part shrank unevenly, cracks developed from the thermal stresses. Cracking can lead to the part completely breaking in either the binder burnout or sintering process. This is shown and further discussed later on in the thesis.

4.3.2. SEM Analysis. Scanning electron microscope images were taken to observe the microstructure of the parts. Polished, fractured, and epoxy-saturated-polished images were taken in the middle of the center of the bar as indicated in Figure 4.9 by the gray dot. Images of the free surface were also taken at the center of one bar on an outer face.

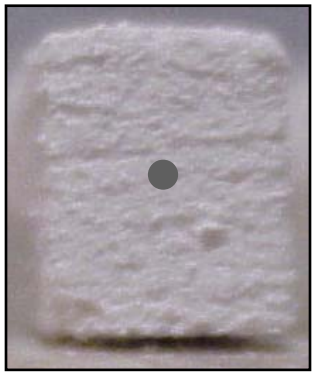

Figure 4.9: Location for polished and fractured surface SEM images

Cracks of a fractured surface propagate through both grain boundaries and the grains themselves. The fractured sintered surface can be seen in Figure 4.10. The pore distribution of the bar is best seen in the epoxy-saturated-polished sample shown in Figure 4.11. This is a thin slice of the part coated with epoxy to fill in all of the pores, making them darker than the alumina. A thick polished section of the sample was also taken (Figure 4.12). Figure 4.13 shows the free sintered surface of the test bar. Figure 4.14 shows the grain structure of the free sintered surface. Low, medium, and high magnification images were taken to offer multiple perspectives of the captured surface. The relative density of the pictured parts according to Archimedes's method was approximately 69% of the theoretical density – 3.96 g/cm^3.

4.4. COMPLEX GEOMETRIC SHAPES

While the greens bars were undergoing a study of the binder burnout process, attention was given to explore the potential of this powder to produce parts with complex shapes. Two popular demonstration pieces during the Duraform^{TM} learning phase were

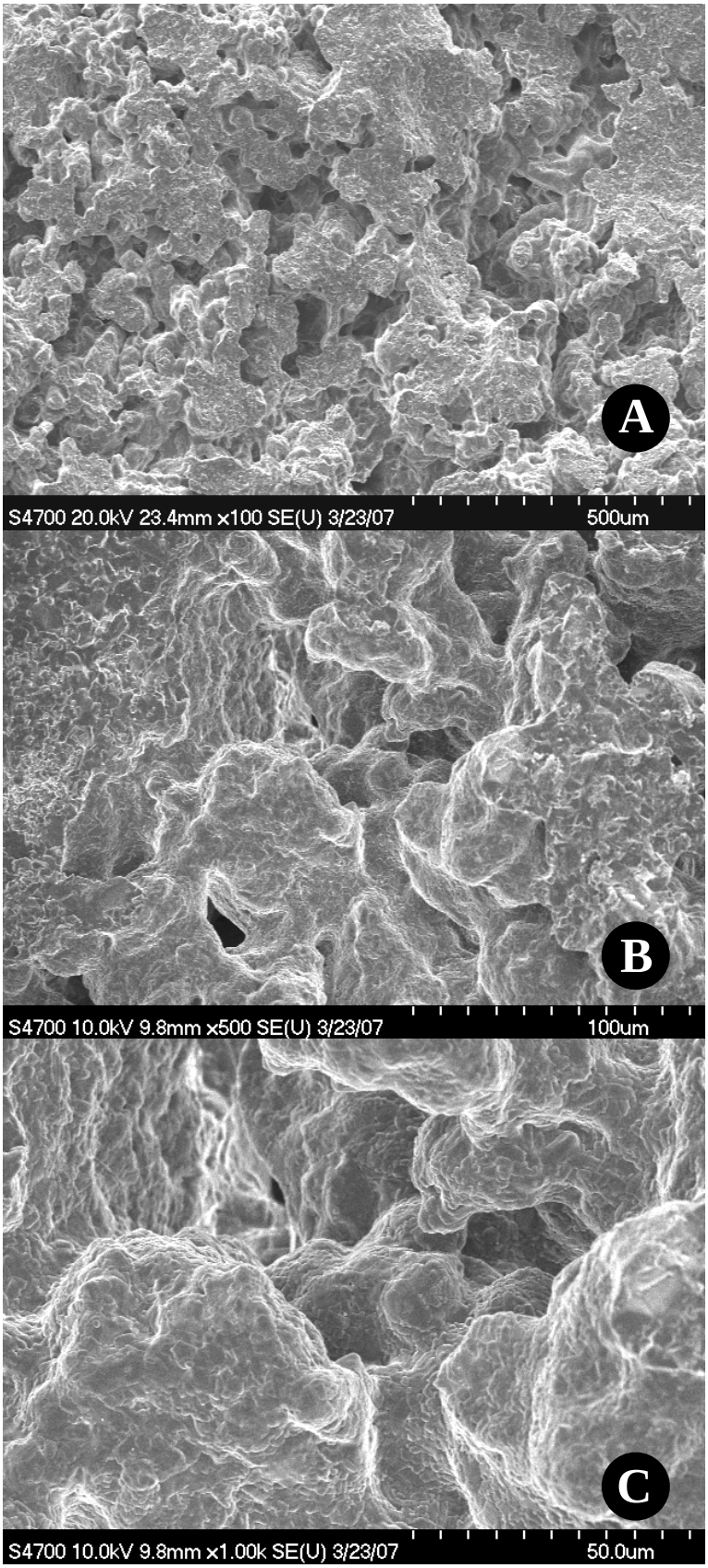

Figure 4.10: Fractured sintered surface: (a) low, (b) medium, and (c) high magnification

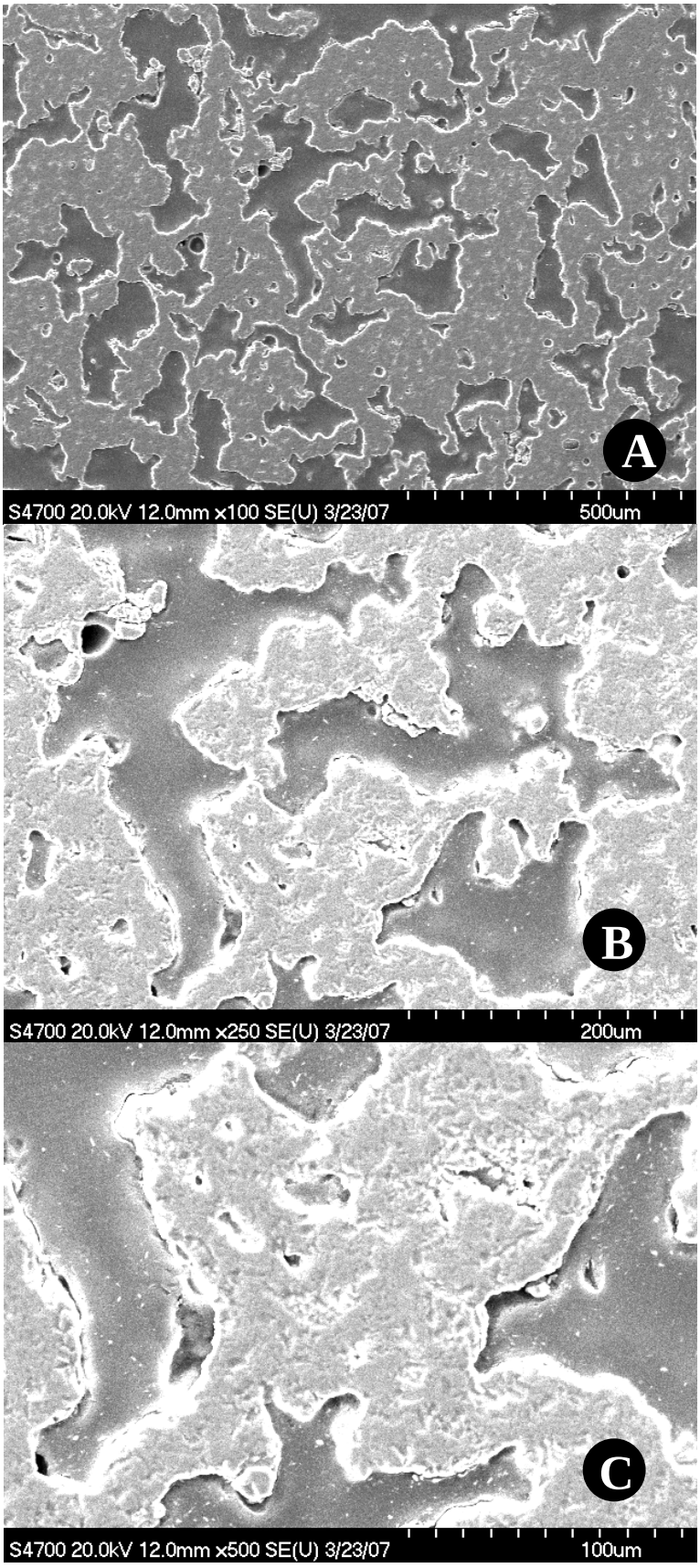

Figure 4.11: Epoxy-saturated sintered surface: (a) low, (b) med., and (c) high mag.

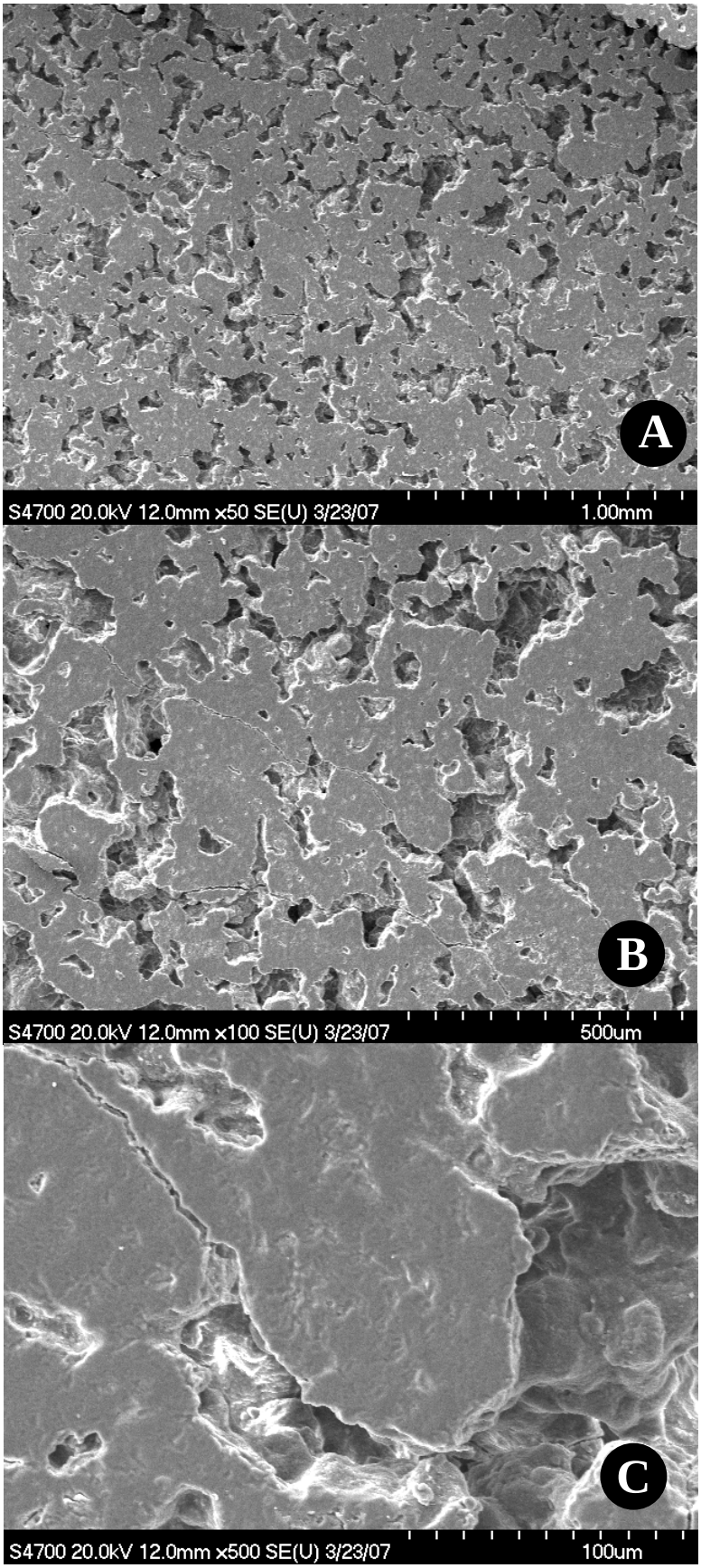

Figure 4.12: Polished sintered surface: (a) low, (b) medium, and (c) high magnification

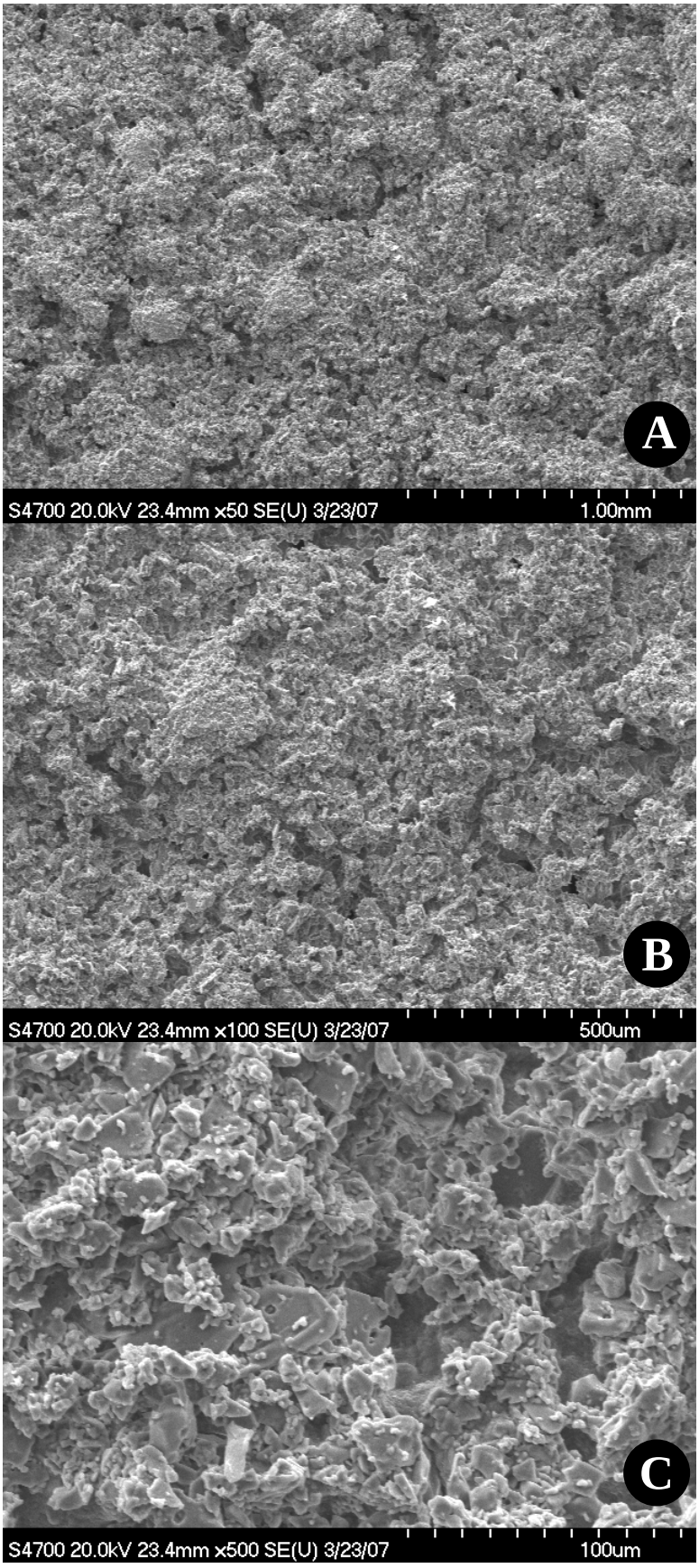

Figure 4.13: Free sintered surface: (a) low, (b) medium, and (c) high magnification

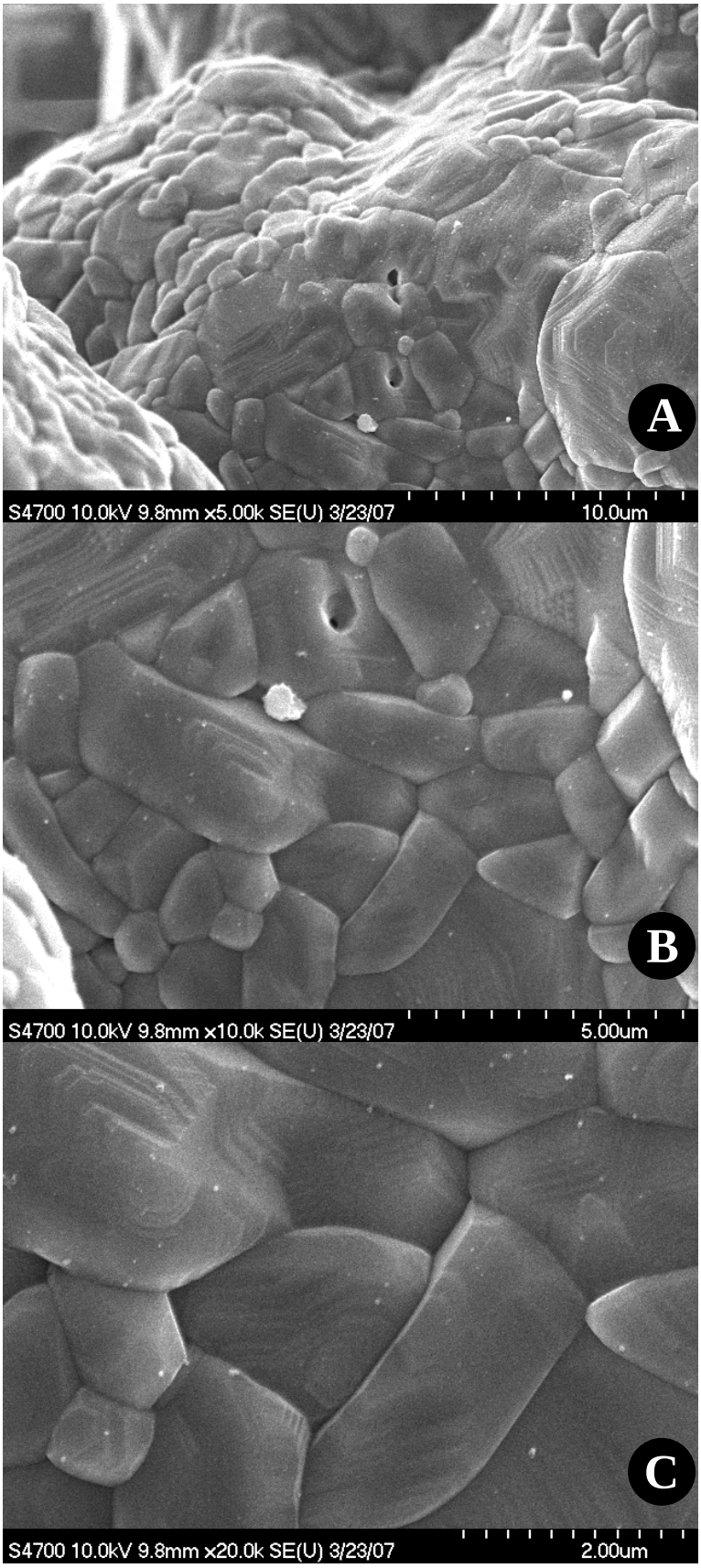

Figure 4.14: Grain structure of free sintered surface: (a) low, (b) med., (c) high mag.

letter bars with the letters “CAMT” or “UMR” and a model airplane on a stand. Slightly modified, these were suitable pieces to test the ability of the ceramic powder and SLS process to produce parts with complex features and to compare the results to those of nylon parts. The STL files of the letter bars and plane are shown in Figure 4.15. An alumina three-link chain was also built to demonstrate the feasibility of producing interconnected ceramic parts with this SLS process.

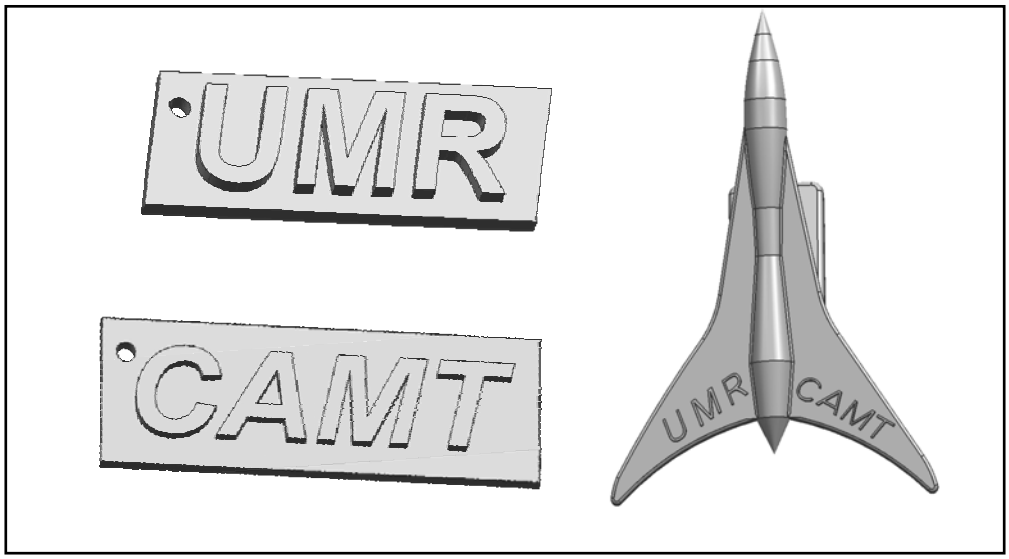

Figure 4.15: Models used to study SLS of ceramic parts with complex geometries

All of the geometries shown were created in Unigraphics (UG) NX3.0. STL files were exported from this software package to be used by the SLS operating software. UG is a powerful 3D CAD software package that enables modeling and analysis of parts created in the software package.

The letter bars were modeled to showcase the ability of the process to produce features in the shape of recognizable forms (letters). Two different sizes were tried to test the level of definition possible for lettering.

The plane exhibits a number of more complex features. The wings overhang the body of the aircraft by approximately three quarters of the total length of the plane. The letters on the wings are thin and small. The nose of the plane is sharply pointed; this feature tests the ability of the powder to support itself in an overhang situation with reducing support from the fused material behind it.

4.4.1. Producing Green Letter Bars. The same operating and laser parameters used to make the green flexural test bars were used to make the letter bars. The initial results were promising. Using the scaling feature offered in the SLS build center software, parts of different sizes were made to observe any quality differences that may occur between them. Bulging on the bottom of the parts deformed the bars, but all of the other surfaces appeared qualitatively smooth and flat. Figure 4.16 shows some of the letter bars. All of the letters were easily distinguishable. The bottom side of the bars is the side not visible in Figure 4.16. The holes in the smaller pieces have swollen shut due to creeping of the excess heat. This raised the question of what hole limitations existed for different part thicknesses and orientation. Several letter bars were prepared for binder burnout, and successfully sintered.

Figure 4.16: Green letter bars

4.4.2. Producing Green Planes. The planes presented an interesting challenge. The planes produced with the Duraform™ powder had thin wings (~ 0.9 mm) and a thin ring stand (~ 4.5 mm). For the stearic-acid/alumina powder, the part file was modified to make the planes more robust from the start. Lessons learned from the Duraform™ builds identified areas of complication for the new parts. Sacrificial parts were strategically placed in an attempt to provide local heat stabilization to make the non-fused powder temperatures surrounding the laser scan areas more uniform for more successful builds.

At first, several variations of orientations and sacrificial part locations were tried to produce planes with a wingspan of roughly 4 inches, a maximum length of 6 inches, and a height of roughly 2.6 inches. Early results were consistently flawed; cracks always developed near their joint of the wings to body of the plane. The cracking would occur

before the breakout of the part from the build-cake. Longer, more gradual cool-down cycles achieved by increasing the cool-down operation powder layer thickness from 0.1 to 0.2 in and several different orientations and placements of sacrificial parts around the cracking areas helped to prevent the cracks from forming in the large part. Figure 4.17 shows a large plane in its green state. Figure 4.18 shows the placement of sacrificial parts that produced the successful green part. In addition to the heat fence at the bottom of the build, a heat fence was placed at the top of the plane to help provide a uniform cool-down stage. The bars under the wings serve as a miniature heat fence for the overhangs.

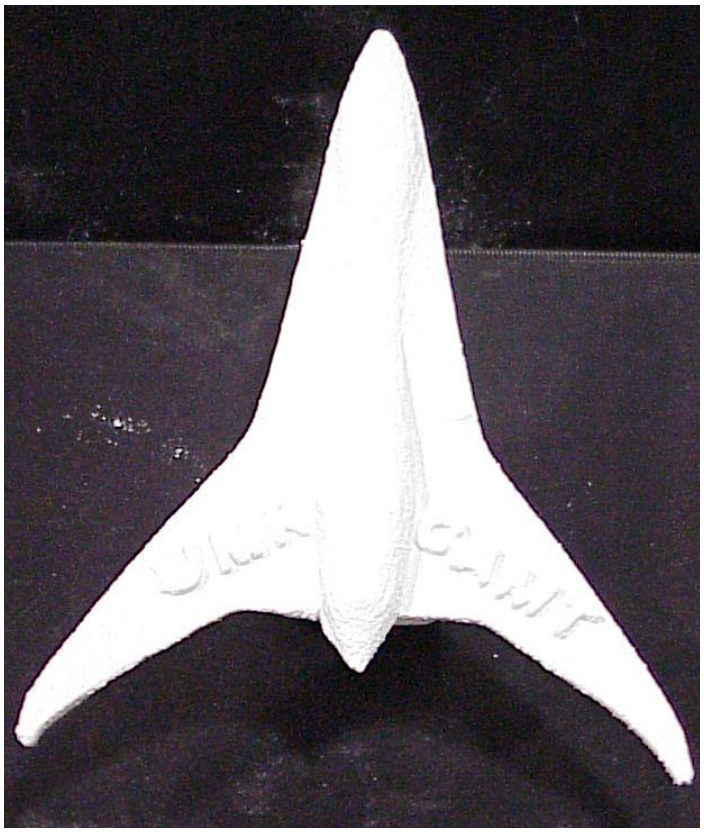

Figure 4.17: Large plane created using SLS and stearic acid/alumina powder

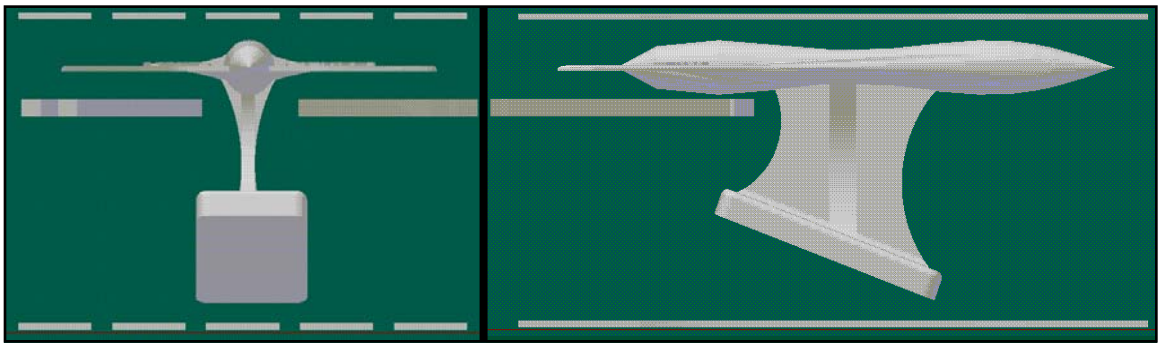

Figure 4.18: Front (left) and side view (right) of sacrificial parts layout for green plane

Another issue with the large planes is the bulging effect, primarily on the bottom of the jet stand. The process alterations discovered from work on the flexural strength test bars were applied to the build, but bulging at the bottom of large surfaces (like the base of the plane) was more severe for the planes than the bars because of the larger scanning area (~ 2,400 mm^2 for the plane base, 540 mm^2 for the fracture bars) that was exposed to cool powder. A tailored laser profile was employed but no noticeable improvements were seen on the parts. Figure 4.19 shows a diagram of the tailored laser power profile for the plane. The areas where bulging was a problem were made using a lower laser power of 4.1 W, where as the weaker sections of the green part were built with a higher laser power of 4.8 W.

The large planes also posed a problem for the binder burnout cycle. The green planes were buried in a crucible using finely ground alumina to support the part throughout the removal of the binder. Planes consistently came out broken like the one shown in Figure 4.20. The length of the binder burnout cycle was increased to 79 hours, and the temperature profile was increased at a slower rate of 0.03 °C/min in order to control the binder removal process and reduce part deformation. However, no large

planes survived the binder burnout process. This was still attributed to issues with binder burnout within the part.

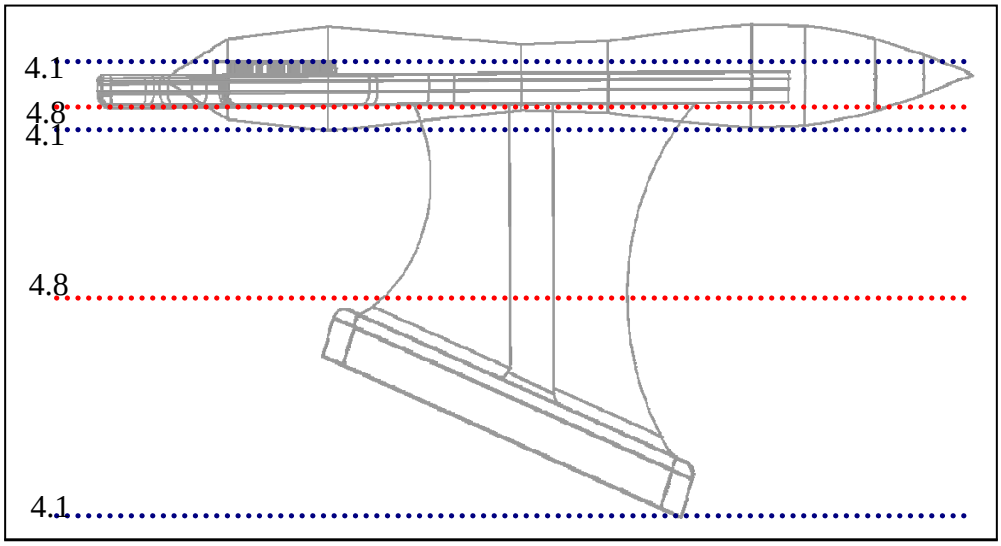

Figure 4.19: Tailored laser power profile for large planes

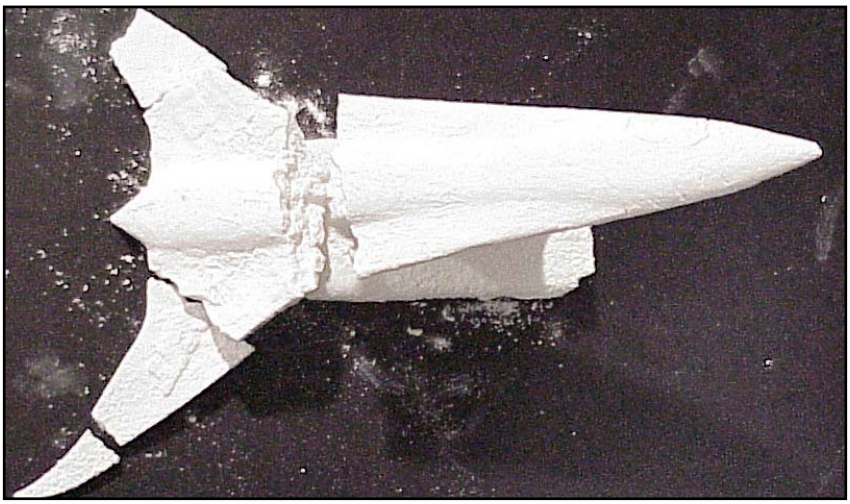

Figure 4.20: Plane broken during binder burnout

Smaller planes, roughly one half scale of the large planes, were built using the same SLS parameters as the large planes (without a tailored laser power profile). These parts initially cracked during binder burnout. Different packing methods for the parts in the crucible and slight adjustment of the binder burnout cycle finally yielded a successful plane. The plane in its green state and after final sintering is shown in Figure 4.21. No parts with greater unsupported overhangs than the small planes were successfully sintered because of the unsuccessful binder burnout of such parts.

Figure 4.21: Green plane (bottom) and fully sintered plane (top)

4.4.3. Producing Alumina Chains. A three-link chain was built to investigate the feasibility of producing interlinked ceramic parts with the SLS process developed in this research. Figure 4.22 shows three different orientations of the chain to demonstrate the independence of each link. The strength of the green and brown part was sufficient for safe breakout, binder burnout, and transport. The successful fabrication of alumina letter bars, model planes, and chains proves the feasibility of the procedures discussed in this thesis to produce parts of complex geometry.

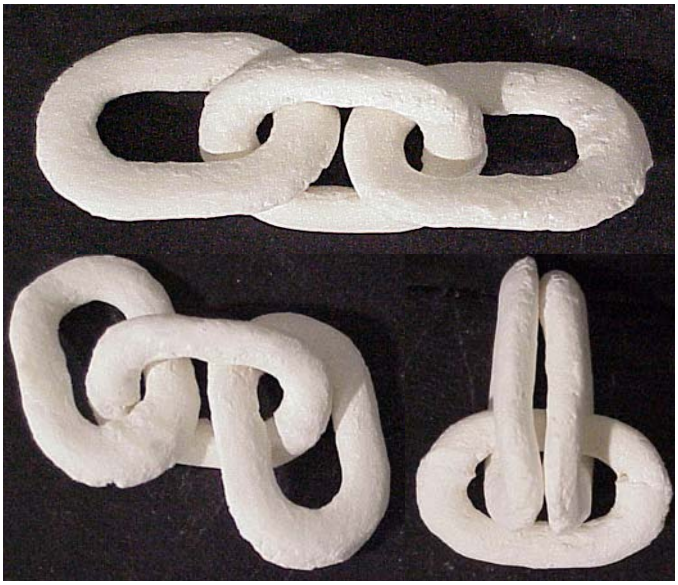

Figure 4.22: Alumina chain links produced by SLS

4.5. HOLED PARTS

The fact that ceramics are brittle materials and have a high hardness value makes them difficult to machine without fracturing. Alumina has a Mohs hardness rating of 9 on a scale where a diamond has a Mohs hardness rating of 10. The use of SLS to make

parts containing through holes has great potential to improve upon industrial hole-making processes. The aim of this study is to explore the capabilities of the process and material to produce holes of different diameters in parts of different thicknesses. Straight holes and holes that curve through parts are of great interest to industrial practitioners.

4.5.1. Straight Holes. This study examined the feasibility of SLS to produce parts with holes using 50/50 vol % stearic acid/alumina powder. The hole orientation during the build process, part thickness, and shrinkage from sintering significantly influenced the diameter of the hole. To begin the study initiated by holes fabricated in the "UMR" and "CAMT" letter bars, cubes with an array of straight holes on each face, bars with straight holes in one direction, and wedges with straight holes in one direction were created as shown in Figure 4.23.

The smallest hole successfully produced in a green part had a designed diameter of 2 mm. After the SLS and sintering process, the average hole diameter of holes built in the X and Y direction of the machine was less than 1 mm in diameter. Holes that were aligned in the Z direction of the build had a larger reduction in diameter than holes built in any other orientation. The wedge part with holes in it, also pictured in Figure 4.24, was oriented such that the holes were aligned with the z-axis of the machine. Four of these parts were produced. The largest hole in the wedge pictured in Figure 4.23 (right side of picture) was designed with a 7.5 mm diameter. Diameter measurements were not repeatable for holes in the wedge pieces because the inclination, which made measured values unreliable. The wedge piece enabled qualitative analysis of the effects of part thickness on hole diameter.

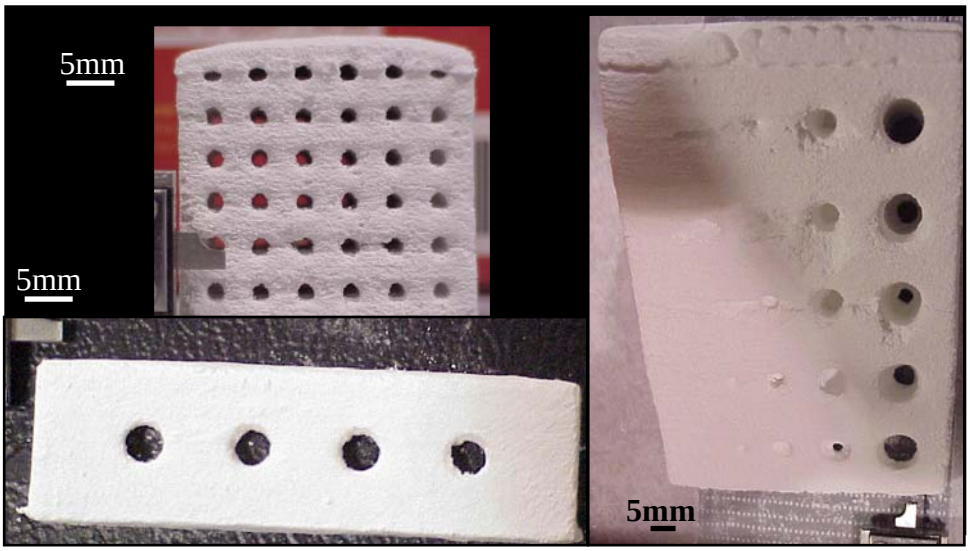

Figure 4.23: Green parts with straight holes

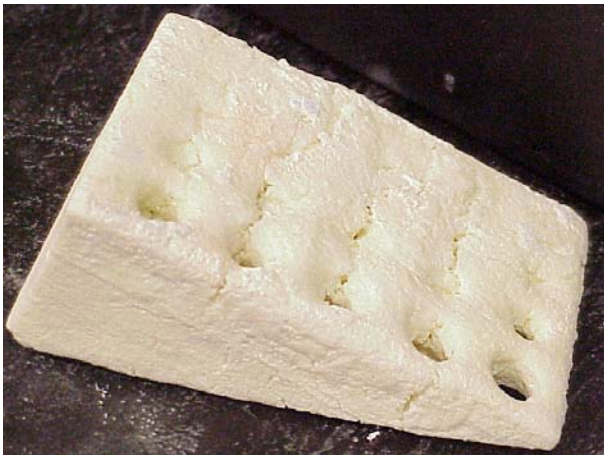

Figure 4.24: Sintered wedge with straight holes

The holes immediately to the left of those as pictured in Figure 4.23 were designed with a 5.25 mm diameter, and only 6 out of 20 of them made it all the way through. The only method used to clear the holes was to blow the parts with 20 psi of air.

Every 5.25 mm hole located at the thinnest part of the wedge resulted in a through hole. Two other 5.25 mm holes located on the second row of holes from the thin edge of the wedge also made it through. The center height of the 5.25 mm holes on the thin edge of the wedge was approximately 8.4 mm. The height of the 5.25 mm circle on the second row from the thin edge of the wedge was approximately 16.12 mm. The holes to the left of the 5.25 mm holes were designed with a diameter of 3.75 mm. The results of these wedges suggested that the maximum height for through-holes between 3.75 and 5.25 mm was less than 8.4 mm. This was considered in future studies of this thesis research.

To investigate this further, the wedge was sintered. Figure 4.25 provides a side-by-side comparison of the green (left) and sintered part (right) with an approximately equal scale factor. The non-fused powder in the middle of the holes densified in the hole during sintering. The comparison between sintered and green part provides some insight as to the diameter and part size reduction. Dimensional measurements of the holes were unreliable because of the angle of the hole surface on the top of the wedge. For that reason, rectangular bars with straight holes in them were made for study.

A study to better characterize the ability of this process to produce holes involves simple coupons with 5 mm diameter holes in them. These bars have been rotated around the machine x-axis to either 30°, 45°, or 60° from vertical. The reasoning for this rotation is two-fold: to minimize bulging and explore the quality of holes that have different exposures in the z-axis direction.

By rotating the coupons on edge as shown in Figure 4.26, the bulging effect is limited to a smaller portion of the bar. This still produces a ridge, but is a successful step in further reducing the undesirable deformations on green parts. Doing this also rotates

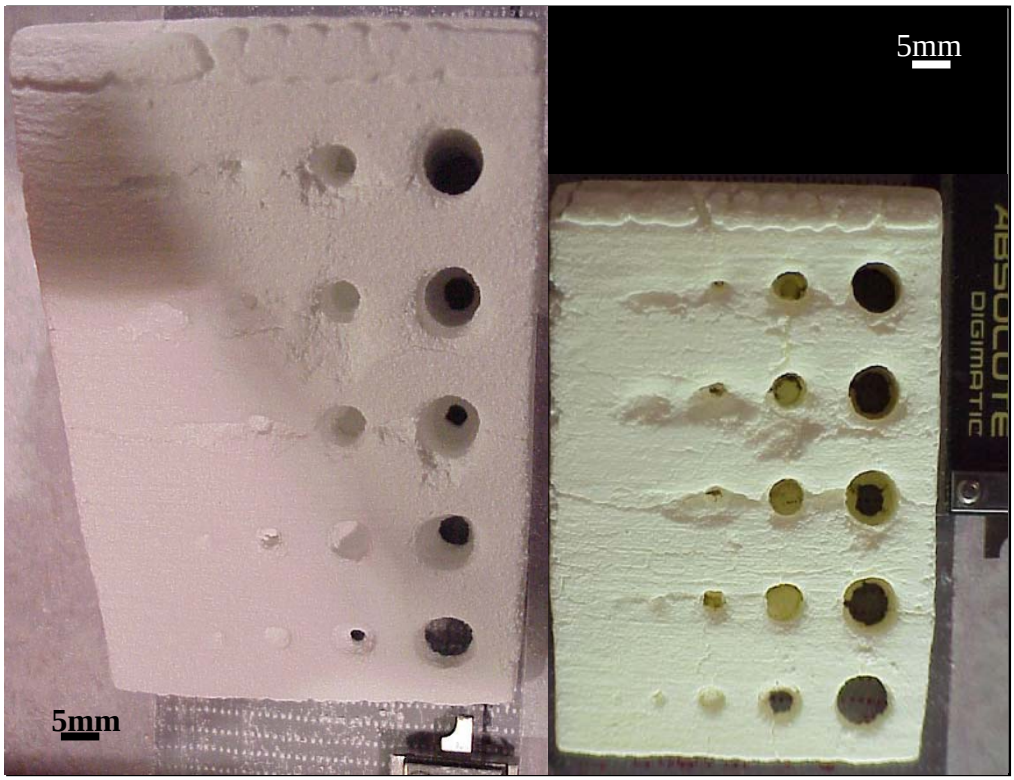

Figure 4.25: Green wedge (left) and sintered wedge (right)

the holes in a less-than-ideal position by exposing holes in varying degrees to the z-direction. The right side of Figure 4.26 shows the difference in orientation between the bar, which are rotated around the x – axis of the SLS machine 30°, 45°, and 60°. Orientations of 0° and 90° were also examined for comparison. The only bars that successfully and consecutively produced 2.5 mm holes were those with hole orientations perpendicular to the z-axis.

Figure 4.27 shows the location of the measurements averaged to determine the diameter of a hole. These measurements were made using magnified photos and pixel measuring software. Four measurements of each diameter were taken at different angles around the hole. For validation, the measurements were repeated in a random order and

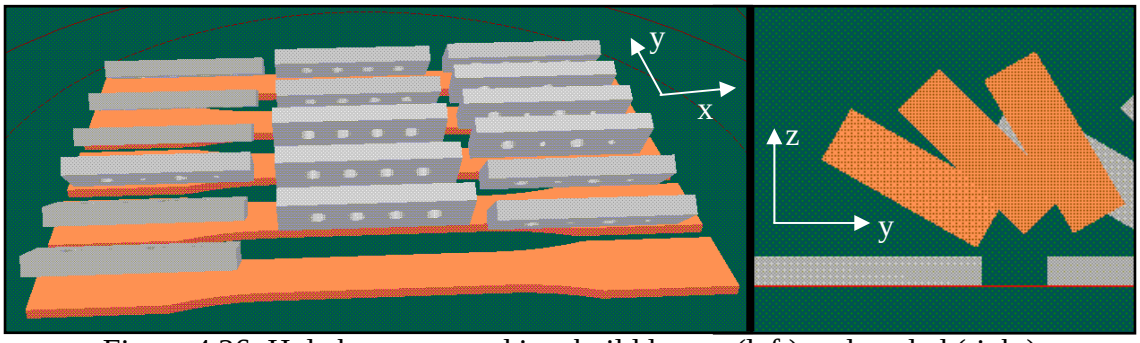

Figure 4.26: Hole bars arranged in a build layout (left) and angled (right)

averaged. Table 4.9 shows average deformations in the form of holes diameter reductions. The diameter reductions were caused by a filling in of the hole from creeping heat. Each hole used in Table 4.9 was designed to have a diameter of 5 mm, but green part hole diameters were reduced to a range of 2.49 to 3.6 mm depending upon the part rotation. The table shows both the physical difference and the percent difference. Some bars had four 5 mm holes on them, and others had two 5 mm holes and two 2.5 mm holes. Every 2.5 mm hole except for holes oriented in a direction perpendicular to the vertical axis sealed shut because of the heat affected zone. The “n/a” for holes in some bars indicates that there were only closed 2.5 mm holes at that location on the bar. The full data set is available for review in Appendix G. Both the upper and lower surface of each coupon was analyzed to observe the variance in the photographs of each side. One observation from this data was that the greater the angle of rotation from vertical, the greater the reduction in hole diameter of the green part. The bar hole diameter reduction was minimized by orienting the hole axis perpendicular to the Z-axis.

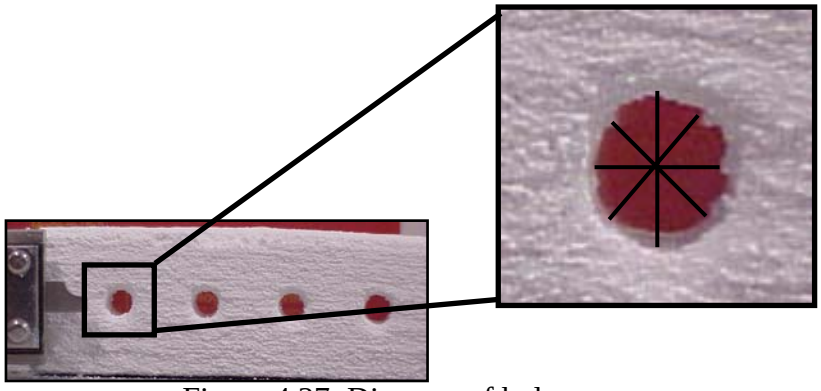

Figure 4.27: Diagram of hole measurements

Table 4.9: Average of hole coupon experimental results

	Left		Mid Left		Mid Right		Right	
Part Rot.	(mm)	(%)	(mm)	(%)	(mm)	(%)	(mm)	(%)
0° from vert.	1.41	28.11	1.44	28.81	1.40	28.01	1.74	34.81
30° from vert.	1.54	30.80	1.54	30.82	1.55	30.95	1.47	29.38
45° from vert.	1.59	31.78	n/a	n/a	1.65	33.09	n/a	n/a
60° from vert.	2.04	40.70	1.92	38.50	1.98	39.51	1.86	37.11
90° from vert.	2.17	43.45	2.01	40.12	2.37	47.47	2.51	50.19

The smallest hole produced in this study was 0.69 mm in a bar thickness of ~6.5 mm. That was in a hole bar oriented with the hole direction perpendicular to the Z-axis. Part thickness has been shown to limit the diameter of producible hole. To our knowledge, the only previous study that worked with the SLS fabrication of holes in zirconia (ZrO_2) bars was able to achieve a hole diameter of 180 µm in a dense part [9].

The part thickness for this hole was 0.381 mm, and infiltration was used to bring the final relative density of this part to approximately 58%.

4.5.2. Curved Holes. Another hole feature looked at in this study is the ability to make hollow bends inside of parts. This can be challenging to do with traditional ceramic processes, but rather simple for typical SLS processes. A 6x21 mm slot and a 6 mm hole were tested in the block shown in Figure 4.28. Both the slot and hole make a 90° bend in the middle of the block. The holes did not make it completely through the part, but the slots did. Every slot created (a total of 8) made it through to its adjacent face, regardless of the orientation of opening face. The shrinkage of the opening was measured in the same fashion as the holes. To show that the slot is a through slot, a piece of string was threaded through the slot (Figure 4.28) both before and after the part was sintered.

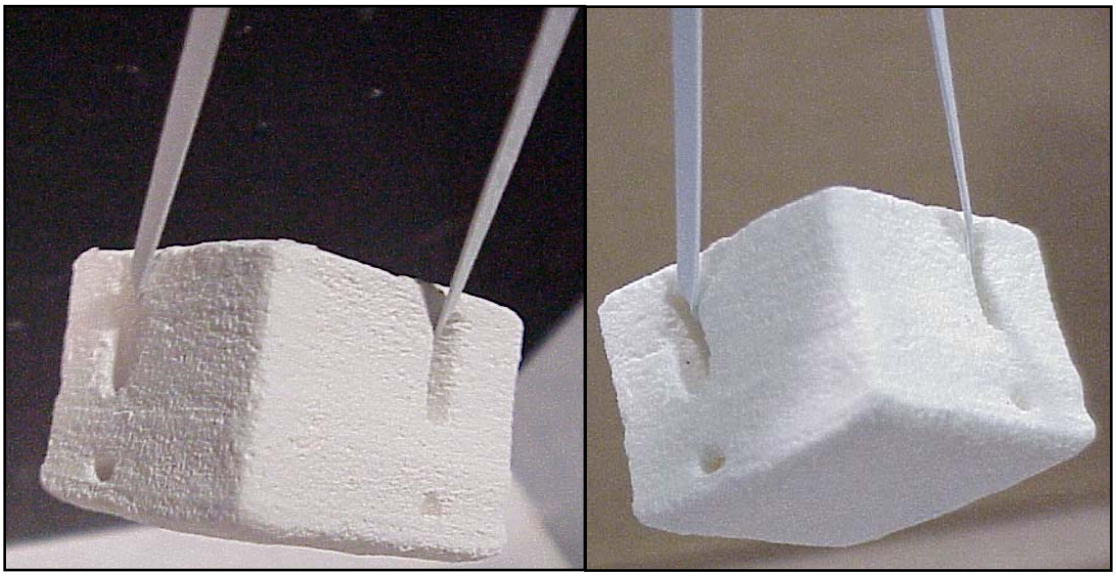

Figure 4.28: Through slot demonstration for (left) brown and (right) dense part

To better illustrate the design of the hole, a 3D and wire-frame rendering of the block is shown in Figure 4.29. Even though the slots weave around each other, no intersection was detected when compressed air was forced through the part.

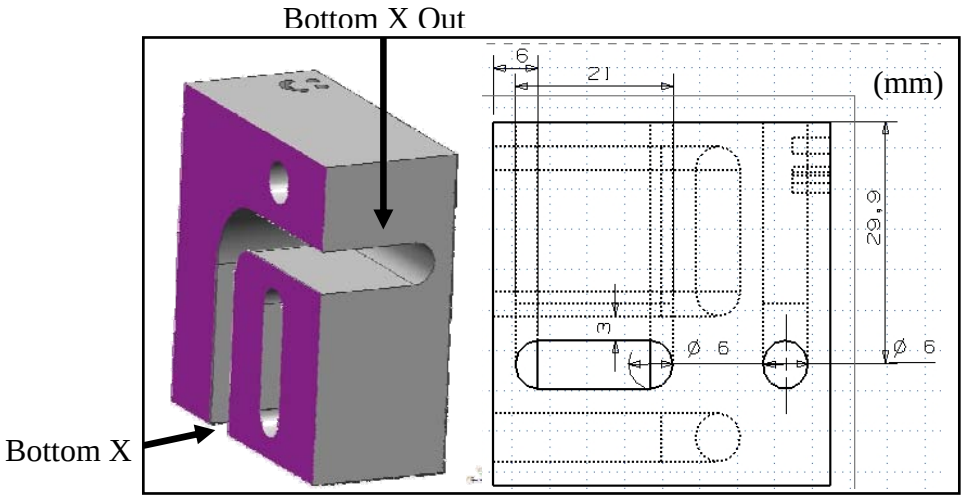

Figure 4.29: 3D model (left) with wire-frame drawing (right) of 90º bend

The face orientation of the slot opening does have an effect on the part. Figure 4.30 shows a chart of the average slot dimension for a face of the green blocks. The results indicate that slot openings on the bottom face of a block shrink more than those that open on any other block face. This was expected and is a result of the bulging issue. To negate this effect, the block can be built at an angle (with a corner or edge of the block being the lowest point of the part). Each slot was measured by 4 measurements, as shown in Figure 4.31; length (L), width at the left end (WL), width in the center (WC), and width at the right end of the slot (WR). Those were then repeated in a random order

to help validate the results. The same 5 mm scale used in other measurements was again used for these. For the raw data used to generate these average values, see Appendix D.

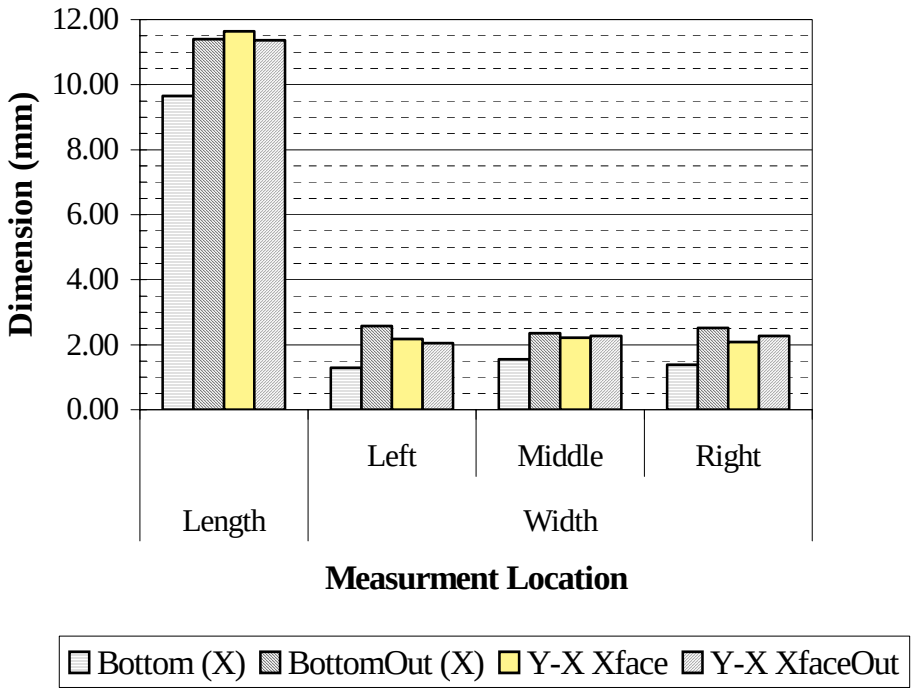

Figure 4.30: Average slot dimensions for a block

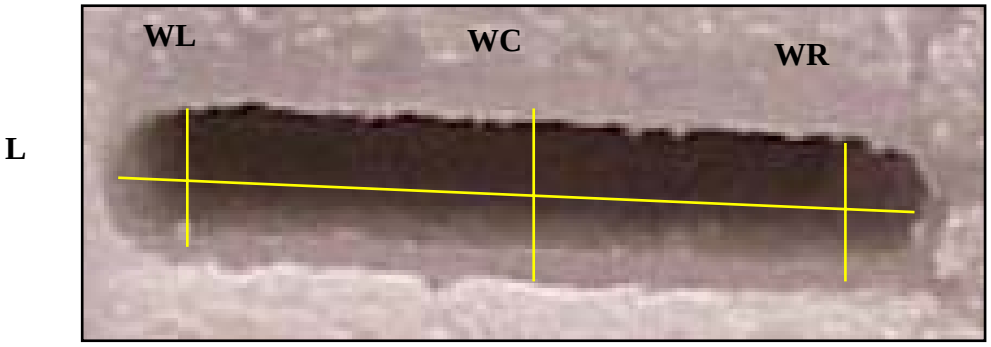

Figure 4.31: Slot measurement guide

The same measurements were taken of sintered blocks. The slots produced inconsistent results. The complete results are in Appendix E. Table 4.10 provides the overall average reduction of the slot compared to the designed dimensions and the average slot variation due to sintering. A more in-depth study is needed to better understand and anticipate the outcome of slot and hole production in these ceramic parts.

Table 4.10: Effects of sintering on slot variation

Block Id:	Length		Average Width	
	(mm)	(% Diff)	(mm)	(% Diff)
2D_S_R_S	0.77	6.83	0.30	17.00
2D_S_F_S	-2.37	-21.49	-0.02	-1.08

A part with a complex multi-bend hole was also successfully built using a design diameter of 8 mm. The part has been sintered, and the hole remains open. Figure 4.32 is the 3D model and wire-frame of the complex hole path inside the thick ceramic block.

4.5.3. Binder Burnout of Holed Parts. Only one thing has to be done differently concerning the binder burnout process for holed parts; the holes have to be cleared after being buried in the crucible. Every other component of the binder burnout process remains the same for these parts. All of these parts were only submitted for binder burnout and sintering. No other post-processing means have been used to alter the characteristics of the parts shown and discussed.

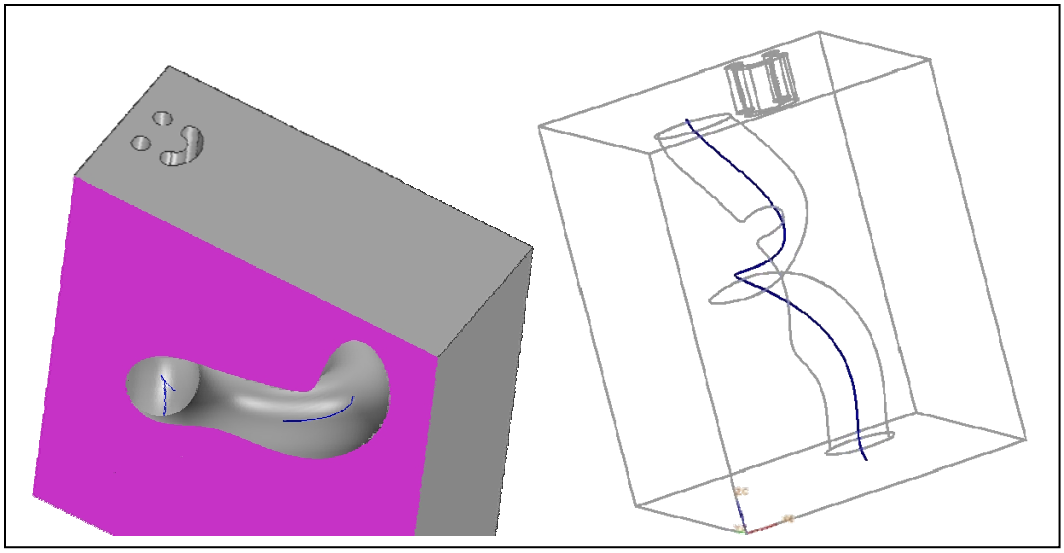

Figure 4.32: 3D model and wire-frame showing complex hole path

4.5.4. Surface Roughness. Surface roughness measurements were performed on 8 flexural test bars that were fused with a laser power of 4.8 W to observe the quality of surface finish obtainable through the processes developed in this research. No polishing or grinding was performed on these specimens prior to these measurements. Each of the 8 test bars was measured three times (once on each end and once in the middle of each bar) on each of the four long sides of the bar. Figure 4.33 illustrates the measurement locations on one of the four sides. These measurements were not repeated because the initial measurements slightly scarred the parts, which would skew the results for the second measurement. The individual results for each bar are listed in Appendix F. The overall average surface roughness for the test bars is approximately 7.6 µm. This is comparable to rough-cut machining operations such as shaping, boring, turning, and electric discharge machining. Surface roughness measurements of SLS nylon parts made in this thesis study had an average surface roughness value of 10.6 µm. Parts produced in

study done by Reddy to optimize SLS parameters for Duraform PA (polymide) yielded an average surface roughness value of 11 µm [19].

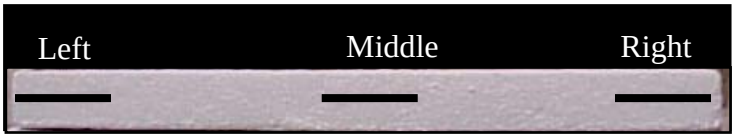

Figure 4.33: Surface roughness measurement locations on test bar

Finer surface roughness values are achievable by machining green blanks. When diamond tooling is used to shape blanks, Ra values of 0.3 µm are possible after sintering. The tooling for this result was a diamond-coated flat-end mill bit. Prior to sintering, the surface roughness is reported to be between 2.3 and 3.1 µm depending upon the method used to form the alumina blank [4]. Ultrasonic machining techniques can also be applied to ceramic blanks. The resulting surface roughness values for such operations range from ~ 3.8 to 6.7 µm [12]. The surface roughness of the sintered alumina parts created by SLS is not yet comparable to that of machined ceramic parts.

5. CONCLUSIONS

This research has shown that stearic acid is a capable binder to use with alumina for SLS. Parts of complex geometries can be produced and sintered with this powder. Green strengths are sufficient for safe handling, and an average sintered density of 88% of the theoretical value for sintered alumina is a significant improvement over any other published result using traditional SLS machines to create dense ceramic parts. The average flexural strength of 255 MPa is also a significant accomplishment of this research, the likes of which are comparable to some industry-produced parts. Note that the flexural strength of an 85% alumina vitreous body ranges from 205 to 310 MPa [29]. An average flexural strength of a 99.9% alumina part is approximately 400 MPa [30]. The average surface roughness of the flexural test bars is approximately 7.6 μm without any finishing processes such as grinding or polishing.

The processes developed in this research have the potential to greatly reduce the time it takes to go from a CAD model to a green part. Traditional methods of binder burnout and sintering are applicable to the green parts produced through this process.

The stearic acid/alumina powder is simple to mix in large quantities and easy to produce in the range of particle sizes currently used for industrial SLS machines. The low melting temperature of the binder and its strong hydroxyl bond to oxide ceramics make it SLS friendly.

The demonstrated abilities of this project to make straight holes as well as holes with sharp bends increase the significance of this work. Parts made from high-temperature ceramics that contain various thicknesses and shapes involving overhangs and complex hole paths can be feasibly made. This could prove to be a significant

improvement to current industrial capabilities. Traditional ceramic post processing techniques such as polishing can be applied to these parts as well for increased dimensional accuracy and better surface finish.

Another encouraging aspect of this research is that all of the equipment necessary to perform these tasks is commercially available. Combining this with the fact that the full capabilities of this technology have yet to be fully realized make this an attractive process to for future study.

6. FUTURE WORK

The groundwork has been laid for future development of stearic acid as a binder for the SLS of ceramic powders. Alumina was the ceramic of choice for the initial stages of this study, and there are still many things to be investigated using the same binder and ceramic combination as in this research. However, the limits of this binder and the full capabilities of the process are far from realized. Below are a few descriptions of further research that need to be done to fully realize the full potential of this research project.

6.1. SLS PROCESS IMPROVEMENTS

The ongoing work to minimize the effects of bulging will continue to improve the ability of SLS to produce dimensionally accurate parts using stearic acid-alumina powder. Further refinement of the SLS operating parameters will be explored to document any potential improvement to the process. Parameters such as scan speed, layer thickness, scan spacing, and laser power need to be optimized for this powder.

6.2. BINDER IMPROVEMENTS

Different methods of coating the ceramic need to be explored to determine the ideal method to create as dense and strong of a part as possible. Other ceramics like zirconia could be investigated to realize the full potential of stearic acid as a binder. Research has begun into the potential advantages of dissolving stearic acid in alcohol and slowly adding the ceramic to the mix. The powder is then vacuum dried and crushed to a size appropriate for SLS operations. Research is needed to compare SLS of alumina

powder produced using this technique with the dry-mixed alumina powder produced using the technique discussed in this thesis.

6.3. STUDY THE THERMODYNAMICS FOR SLS GREEN PARTS

The predominant thermodynamic principles governing the reaction between the stearic acid and alumina when the laser strikes the powder need to be studied to provide an analytical model of the green part production process. This is important to the future development of process parameters and powder combinations. Understanding the complex thermodynamics involved can provide more insight into the ideal parameters for highly accurate part geometries.

6.4. BINDER BURNOUT IMPROVEMENTS

The study of binder burnout and sintering methods needs to be continued to find the best means of creating the best ceramic parts possible. Techniques to encourage more uniform shrinkage of parts during binder burnout should be researched. The need for the ability to produce large parts similar in size to a large plane described in this thesis is a strong driving force for the continuance of this study.

6.5. OTHER POST-PROCESSING OPTIONS

The use of isostatic compaction to densify green parts may yield density and strength values closer to that of ideal parts. Infiltration may also be used to further increase the density and strength of sintered parts. Three flexural strength bars have been made for the initial examination of benefits isostatic compaction may offer. Green parts

are compacted with the anticipation that the compaction will increase the density and strength of the parts after sintering.

6.6. MACHINABILITY STUDY

The parts after completing binder burnout are stronger than the green parts, but not nearly as tough as the sintered parts. This may provide a material that can be easily polished or machined with traditional techniques. The machined parts can then be sintered to achieve maximum density and strength while retaining the improved surface features.

6.7. APPLICATIONS TO ULTRA-HIGH TEMPERATURE CERAMICS

The potential of this binder and process for ultra-high-temperature ceramics (UHTC) applications is unknown. This phase of the study will determine if stearic acid is a feasible binder without the assistance of the hydroxyl bond. Zirconium diboride (ZrB_2) is an UHTC candidate for this area of research.

APPENDIX A.
SINTERSTATION 2000 OPERATING PARAMETERS

The tables in Appendix A give the total range of operating parameters available for adjustment on the SinterStation2000 for both the build and part parameters. Also shown are the ranges of values for each parameter used in this research for the stearic acid/alumina powder. Table A.1 shows the range of thicknesses used for the warm-up and cool-down stages of a build. It also shows the max build height available. Table A.2 shows the complete range of values used in this research for the build parameters. Table A.3 shows the selected build parameter values, and Table A.4 shows both the range of experimental values and the selected values for the part parameters. All units are given in standard units. Please note that the laser power values are what was entered into the machine, not the true laser power that the powder and parts were experiencing, which is what was stated in the thesis.

Table A.1: Operation stage thickness

Warm-UP Height	0.100-0.200in
Build Height	16.5in (max w/ warm up and cool down of 0.1in)
Cool-Down Height	0.100-0.2500in

Table A.2: Build parameter range used in stearic acid/alumina experiments

Build Profile Parameters				
Parameter	**Total Range**	**Exp. Range**		
		Warm-Up	**Build**	**Cool-Down**
Chamber Airflow Damper Position	0-100%	100%	100%	100%
Chamber Cooling Set Point	0-75°C	75°C	40°C	50°C
Chamber Cooling Wait for Temp	No-Yes	No	No	No
Downdraft Enabled	Off-On	Off	Off	Off
Custom Downdraft Enabled	Off-On	Off	Off	Off
Left Feed Distance	0-0.25in	0.012-0.015in	0.012-0.016in	0.008-0.015in
Left Feed Heater Output Limit	0-100%	44%	44%	33-0%
Left Feed Heater Set Point	0-240°C	25-40°C	37-40°C	40-25°C
Left Feed Heater Wait for Temp	No-Yes	Yes	Yes	No
Minimum Time between Layers	0-1200s	15s	10s	10s
Part Heater PID Output Limit	0-100%	44%	44%	33%
Part Heater PID Set Point	0-240°C	35-62°C	58-63°C	63-25°C
Part Heater Wait for Temp	Off-On	On	On	Off
Piston Heater Enable	Off-On	On	On	Off
Piston Heater Output Limit	0-100%	50%	50%	50%
Piston Heater PID Set Point	0-160°C	40-62°C	50-62°C	62-25°C
Powder Layer Delay	0-30s	0s	0s	0s
Powder Layer Thickness	0.003-0.02in	0.005in	0.005in	0.005in
Right Feed Distance	0-0.25in	0.012-0.015in	0.012-0.016in	0.008-0.015in
Right Feed Heater Output Limit	0-100%	44%	44%	33-0%
Right Feed Heater Set Point	0-240°C	25-38°C	37-38°C	38-25°C
Right Feed Heater Wait for Temp	No-Yes	Yes	Yes	No
Roller Speed	3.000-7.000in/s	5.000in/s	5.000in/s	5.000in/s
Rotate Scan Order	Off-On	Off	Off-On	Off

Table A.3: Selected build parameters for stearic acid/alumina powder

Build Profile Parameters				
Parameter	**Total Range**	**Exp. Value**		
		Warm-Up	**Build**	**Cool-Down**
Chamber Airflow Damper Position	0-100%	100%	100%	100%
Chamber Cooling Set Point	0-75°C	75°C	40°C	50°C
Chamber Cooling Wait for Temp	No-Yes	No	No	No
Downdraft Enabled	Off-On	Off	Off	Off
Custom Downdraft Enabled	Off-On	Off	Off	Off
Left Feed Distance	0-0.25in	0.015in	0.016in	0.015in
Left Feed Heater Output Limit	0-100%	44%	44%	33-0%
Left Feed Heater Set Point	0-240°C	25-38°C	38°C	38-25°C
Left Feed Heater Wait for Temp	No-Yes	Yes	Yes	No
Minimum Time between Layers	0-1200s	15s	10s	10s
Part Heater PID Output Limit	0-100%	44%	44%	33%
Part Heater PID Set Point	0-240°C	40-62°C	62°C	63-25°C
Part Heater Wait for Temp	Off-On	On	On	Off
Piston Heater Enable	Off-On	On	On	Off
Piston Heater Output Limit	0-100%	50%	50%	50%
Piston Heater PID Set Point	0-160°C	40-62°C	50-62°C	62-25°C
Powder Layer Delay	0-30s	0s	0s	0s
Powder Layer Thickness	0.003-0.02in	0.005in	0.005in	0.005in
Right Feed Distance	0-0.25in	0.015in	0.016in	0.015in
Right Feed Heater Output Limit	0-100%	44%	44%	33-0%
Right Feed Heater Set Point	0-240°C	25-38°C	38°C	38-25°C
Right Feed Heater Wait for Temp	No-Yes	Yes	Yes	No
Roller Speed	3.000-7.000in/s	5.000in/s	5.000in/s	5.000in/s
Rotate Scan Order	Off-On	Off	Off-On	Off

Table A.4: Range and selected values of part parameters for stearic acid/alumina SLS

Part Profile Parameters			
Parameter	**Total Range**	**Exp. Value**	**Exp. Range**
Max Gap Distance	0-5in	0.100in	0.100in
Fill Laser Power	0-90W	6.000W	4.000-8.000W
Fill Scan Count	0-10	1	1-2
Fill Beam Offset X	-0.02to0.02in	0in	0in
Fill Beam Offset Y	-0.02to0.02in	0in	0in
Fill Jump Delay	2-65534.0µs	1000µs	1000µs
Fill Jump Speed	2-500in/s	200.00in/s	200.00in/s
Fill Laser Off	2-65534.0µs	1500.0µs	1500.0µs
Fill Laser On	20-65534.0µs	1124.0µs	1124.0µs
Fill Scan Delay	2-65534.0µs	36.0µs	36.0µs
Fill Scan Speed	2-500in/s	35in/s	35in/s
Outline Laser Power	0-90W	5.000W	4.000-8.000W
Outline Scan Count	0-10	1	1-2
Outline Beam Offset X	-0.02to0.02in	0	0
Outline Beam Offset Y	-0.02to0.02in	0	0
Outline Jump Distance	2-65534.0us	500us	500µs
Outline Jump Speed	2-500in/s	60.000in/s	60.000in/s
Outline Laser Off	2-65534.0µs	1500.0µs	1500.0us
Outline Laser On	20-65534.0µs	1124.0µs	1124.0us
Outline Scan Delay	2-65534.0µs	36.0µs	36.0µs
Outline Scan Speed	2-500in/s	11.000in/s	11.000-20.000in/s
Slicer Fill First	Off-On	On	On
Slicer Fill Scan Spacing	0.003-1in	0.005in	0.005-0.006in
Sorted Fill Enabled	Off-On	Off	Off-On
Sorted Fill Max Jump	0.1-16.0in	0.500in	0.005in

APPENDIX B.
PMMA SLS PROCESS PARAMETERS

PMMA was not chosen as a binder for fine alumina ceramic due to the inability to produce green parts that could support their full weight. Table B.1 and B.2 lists the parameters tried. All listed dates are in 2006. Below is a list of parameter descriptions.

Part Temperature – Temperature of the powder in the part build area

Feed Temperature – Temperature of the feed powder on either side of the part build chamber

Piston Temperature – Temperature of the heater under the part build area

Laser Power – The set laser power of the machine for experimentation

Laser Spacing – Distance between laser raster paths when scanning a profile

Laser Speed – The speed at which the laser rasters

Laser Scan Count – The number of times the laser scans a profile

Build Feed – The height of the feed containers elevated to allow the roller to spread a fresh layer of powder

Build Layer – Distance the part cylinder moves down to allow a new layer of material to be spread

Table B.1: PMMA experimentation parameters 2006

	Temperature Parameters			Laser Parameters				Build Parameters	
Date	Part (°C)	Feed (°C)	Piston (°C)	Power (Watts)	Spacing (in)	Speed (in/s)	Scan Count	Feed (in)	Layer (in)
13-Jul	110	35	90	7	0.004	30	1	0.008	0.004
	110	35	90	8	0.004	30	1	0.008	0.004
	110	35	90	9	0.006	30	1	0.008	0.004
14-Jul	130	35	90	7	0.004	30	1	0.008	0.004
	130	35	90	8	0.004	30	1	0.008	0.004
	130	35	90	9	0.006	30	1	0.008	0.004
17-Jul	110	35	90	12	0.006	50	1	0.008	0.003
	110	35	90	5	0.004	30	2	0.008	0.003
	110	35	90	7	0.006	30	2	0.008	0.003
18-Jul	110	35	80	12	0.006	75	3	0.0098	0.004
	110	35	80	4	0.004	30	5	0.0098	0.004
	110	35	80	7	0.006	30	2	0.0098	0.004
19-Jul	110	35	80	12	0.006	75	3	0.013	0.004
	110	35	80	4	0.004	30	5	0.013	0.004
	110	35	80	7	0.006	30	5	0.013	0.004

Table B.2: PMMA experimentation parameters 2006 continued

Date	Powder Type	Temperature Parameters			Laser Parameters		
		Part (°C)	Feed (°C)	Piston (°C)	Power (Watts)	Spacing (in)	Speed (in/s)
30-May	Alumina/PMMA	178	80	133	9.5	0.06	50
31-May	Alumina/PMMA	130	60	130	12, 25	0.06	50
1-Jun	Alumina/PMMA	200	150	150	8.5	0.06	50
5-Jun	Alumina/PMMA	235	140	150	8.5	0.06	50
6-Jun	Alumina/Nylon	178	80	133	14.5, 15.5, 16.5	0.06	50
7-Jun	Alumina/Nylon	178	80	133	14.5, 15.5, 16.6	0.06	50
15-Jun	Alumina/Nylon	178	80	133	16	0.03	20, 25, 30
16-Jun	Alumina/Nylon	178	80	133	16	0.03	20, 25, 30
17-Jun	Alumina/Nylon	178	80	133	8, 11, 14	0.03	20
19-Jun	Alumina/PMMA	200	135	150	9, 11, 13	0.03	20, 25, 30
20-Jun	Alumina/PMMA	130	100	130	7, 8, 9	0.03	20, 15, 10
21-Jun	Alumina/PMMA	120	75	120	7, 8, 9	0.03	20, 15, 10

APPENDIX C.

RAW DATA FOR FLEXURAL TEST BAR SHRINKAGE

This data in this appendix is of green and sintered flexural test bars. Table C.1 provides data for one batch of green test bars. Table C.2 provides the same information for green bars of a different build. Both builds were sintered, but only the bars listed in Table C.3 made it through the binder burnout and sintering process. The numbers for bars in Table C.3 are for reference purposes only. Table C.4 shows the overall shrinkages of the bars from the green state to the sintered bar.

Table C.1: Measurements are of green parts built on Sept. 15, 2006

	Center Width (mm)			Length (mm)			Height (mm)		
	M1	M2	AVG	M1	M2	AVG	M1	M2	AVG
Laser Power = 4.1W	8.93	9.14	9.035	93.24	92.16	92.70	10.87	10.71	10.79
	9.01	8.91	8.96	92.68	93.03	92.855	10.75	10.78	10.765
	8.85	8.78	8.815	93.02	92.42	92.72	10.94	10.83	10.885
	8.24	8.52	8.38	95.06	94.61	94.835	9.27	9.37	9.32
	9.05	8.89	8.97	92.62	92.24	92.43	10.93	11.1	11.015
	8.73	8.71	8.72	93.2	93.08	93.14	10.33	10.3	10.315
	8.31	8.66	8.485	92.56	92.85	92.705	10.4	10.58	10.49
	10.42	10.36	10.39	94.25	94.32	94.285	8.23	8.15	8.19
	8.64	8.21	8.425	93.47	92.17	92.82	9.97	10.05	10.01
	Total Avg =		8.91	Total Avg =		93.17	Total Avg =		10.20
Laser Power = 4.8W	10.2	10.1	10.15	94.59	94.67	94.63	11.2	11.29	11.245
	11.04	11	11.02	93.62	94.12	93.87	9.21	9.04	9.125
	10.88	10.77	10.825	93.06	93.66	93.36	8.74	8.65	8.695
	8.89	8.85	8.87	93.11	92.94	93.025	10.48	10.55	10.515
	10.16	10.2	10.18	94.8	94.48	94.64	10.91	10.95	10.93
	9.93	9.93	9.93	94.11	93.56	93.835	11.29	11.18	11.235
	8.81	8.73	8.77	92.76	92.94	92.85	10.15	9.95	10.05
	10.51	10.66	10.585	94.64	94.79	94.715	11.94	12.05	11.995
	10.35	10.58	10.465	94.48	94.72	94.60	11.87	11.9	11.885
	Total Avg =		10.09	Total Avg =		93.95	Total Avg =		10.63
Laser Power = 6.2W	13.66	13.26	13.46	95.09	95.08	95.085	10.57	10.46	10.515
	10.06	10	10.03	94.17	94.34	94.255	11.21	11.41	11.31
	9.86	9.92	9.89	94.74	94.88	94.81	11.8	11.94	11.87
	13.97	14.05	14.01	96.47	96.36	96.415	15.48	15.21	15.345
	13.34	13.24	13.29	95.16	95.12	95.14	9.94	9.84	9.89
	Total Avg =		12.14	Total Avg =		95.14	Total Avg =		11.79

Table C.2: Measurements are of green parts built on Sept. 19, 2006

	Center Width (mm)			Length (mm)			Height (mm)		
	M1	M2	AVG	M1	M2	AVG	M1	M2	AVG
Laser Power = 4.1W	7.51	7.42	7.47	92.80	92.32	92.56	9.03	9.11	9.07
	7.82	7.71	7.77	92.82	92.60	92.71	9.92	9.85	9.89
	7.70	7.67	7.69	92.81	92.62	92.72	9.83	9.68	9.76
	7.66	7.67	7.67	92.57	92.44	92.51	9.83	9.60	9.72
	7.72	7.65	7.69	92.76	92.51	92.64	9.84	9.70	9.77
	7.61	7.61	7.61	92.86	92.41	92.64	9.57	9.56	9.57
	7.69	7.60	7.65	92.66	92.48	92.57	9.69	9.85	9.77
	7.46	7.52	7.49	92.87	92.81	92.84	9.25	9.21	9.23
	7.50	7.50	7.50	92.49	92.32	92.41	8.69	8.86	8.78
	7.38	7.54	7.46	94.00	93.93	93.97	9.53	9.64	9.59
	Total Average =		7.60	Total Average =		92.75	Total Average =		9.51
Laser Power = 4.8W	7.55	7.80	7.68	93.20	93.15	93.18	9.72	9.69	9.71
	7.82	7.81	7.82	93.25	93.24	93.25	9.73	9.57	9.65
	8.05	8.07	8.06	93.18	93.18	93.18	9.99	9.97	9.98
	7.64	7.64	7.64	92.50	92.45	92.48	9.64	9.61	9.63
	8.15	8.22	8.19	93.38	93.35	93.37	9.98	10.04	10.01
	8.27	8.26	8.27	93.63	93.65	93.64	10.10	10.11	10.11
	8.34	8.30	8.32	93.64	93.69	93.67	10.26	10.28	10.27
	8.31	8.29	8.30	93.71	93.70	93.71	10.39	10.37	10.38
	8.22	8.16	8.19	93.69	93.67	93.68	10.12	10.21	10.17
	8.30	8.34	8.32	93.70	93.70	93.70	10.42	10.48	10.45
	7.91	8.01	7.96	93.50	93.60	93.55	9.93	10.08	10.01
	7.59	7.54	7.57	92.41	92.40	92.41	9.74	9.67	9.71
	Total Average =		8.02	Total Average =		93.32	Total Average =		10.00
Laser Power = 6.2W	8.78	8.76	8.77	94.40	94.36	94.38	10.46	10.42	10.42
	8.76	8.62	8.69	94.39	94.34	94.37	10.72	10.56	10.56
	8.42	8.38	8.40	93.55	93.62	93.59	10.59	10.57	10.57
	9.79	9.83	9.81	94.20	94.26	94.23	11.02	11.00	11.00
	10.28	10.29	10.29	94.51	94.43	94.47	11.87	11.66	11.66
	10.55	10.50	10.53	94.54	94.71	94.63	10.55	12.01	12.03
	10.17	10.12	10.15	94.41	94.41	94.41	10.17	12.15	12.05
	9.75	9.73	9.74	93.98	93.89	93.94	11.25	11.25	11.15
	10.40	10.29	10.35	94.07	94.00	94.04	9.98	9.98	10.08
	10.11	10.03	10.07	94.40	94.19	94.30	11.87	11.87	12.08
	8.48	8.51	8.50	93.12	93.19	93.16	10.64	10.64	10.62
	Total Average =		9.57	Total Average =		94.14	Total Average =		11.11

Table C.3: Measurement of sintered parts from builds completed Sept. 15 & 19, 2006

4.1W	Length (mm)		Avg	Width (mm)		Avg	Height (mm)		Avg
Na	77.92	78.17	78.05	5.97	5.95	5.96	7.25	7.22	7.24
Na	77.28	77.64	77.46	6.17	6.09	6.13	7.08	7.02	7.05
Na	78.54	78.60	78.57	5.68	5.64	5.66	7.52	7.57	7.55
Na	77.77	77.87	77.82	6.12	6.02	6.07	7.33	7.35	7.34
Na	77.47	77.53	77.50	5.90	5.87	5.89	6.93	6.86	6.90
Na	77.84	78.42	78.13	5.94	5.89	5.92	7.18	7.16	7.17
Na	77.81	77.84	77.83	6.03	6.01	6.02	7.18	7.25	7.22
		Avg	77.91		Avg	5.95		Avg	7.21
4.8W									
1	78.31	78.34	78.33	6.85	6.59	6.72	7.68	7.74	7.71
2	78.13	78.20	78.17	6.63	6.70	6.67	7.93	8.03	7.98
3	78.13	78.13	78.13	6.54	6.57	6.56	7.55	7.57	7.56
4	78.17	78.13	78.15	6.59	6.62	6.61	7.65	7.56	7.61
5	78.35	78.35	78.35	6.11	6.03	6.07	7.80	7.83	7.82
6	78.17	78.00	78.09	6.78	6.71	6.75	7.72	7.69	7.71
7	78.16	78.19	78.18	6.51	6.50	6.51	7.67	7.69	7.68
8	78.35	78.38	78.37	6.69	6.74	6.72	7.94	7.88	7.91
9	77.75	77.82	77.79	6.19	6.20	6.20	7.29	7.45	7.37
10	77.98	77.91	77.95	6.50	6.47	6.49	7.59	7.57	7.58
11	77.79	77.83	77.81	6.24	6.24	6.24	7.76	7.51	7.64
12	78.39	78.49	78.44	6.16	6.17	6.17	7.85	7.84	7.85
		Avg	78.14		Avg	6.47		Avg	7.70
6.2W									
1	77.91	78.05	77.98	6.82	6.81	6.82	7.87	7.86	7.87
2	78.31	78.07	78.19	6.64	6.66	6.65	8.19	8.08	8.14
		Avg	78.09		Avg	6.73		Avg	8.00

Table C.4: Weights and rough densities of green flexural test bars

4.1W	Weight (g)		Avg	Density (g/cm^3)
Na	7.00	7.00	7.00	2.08
Na	7.00	7.00	7.00	2.09
Na	7.00	7.00	7.00	2.09
Na	7.00	7.00	7.00	2.02
Na	7.00	7.00	7.00	2.23
Na	7.00	7.00	7.00	2.11
Na	7.00	7.00	7.00	2.07
			Avg	2.10

4.8W				
1	9.00	9.00	9.00	2.22
2	9.00	9.00	9.00	2.16
3	9.00	9.00	9.00	2.32
4	8.00	8.00	8.00	2.04
5	7.00	7.00	7.00	1.88
6	9.00	9.00	9.00	2.22
7	9.00	9.00	9.00	2.30
8	9.00	9.00	9.00	2.16
9	7.00	7.00	7.00	1.97
10	8.00	8.00	8.00	2.09
11	7.00	7.00	7.00	1.89
12	8.00	8.00	8.00	2.11
			Avg	2.11

6.2W				
1	8.00	8.00	8.00	1.91
2	9.00	9.00	9.00	2.13
			Avg	2.02

Table C.5: Average shrinkage of the flexural test bars from the green to sintered stage

Average Shrinkage from Green to Sintered Part						
	Length		Width		Height	
LP (Watts)	(mm)	%Diff	(mm)	%Diff	(mm)	%Diff
4.1	14.85	16.0	1.65	21.7	2.30	24.2
4.8	15.17	16.3	1.55	19.3	2.30	23.0
6.2	16.05	17.0	2.84	29.7	3.11	28.0

APPENDIX D.

RAW DATA FOR SLOT SHRINKAGE OF GREEN PARTS

Table D.1 measures the slots in the green blocks made for a feasibility study concerning the ability of ceramic parts containing complex holes to be fabricated using SLS. Table D.2 shows the same data taken from a different block of the same design, but with a different part orientation.

The top four sections of Table D.1 separated by a thick line are four sides of the slotted-cube that had slot openings. Each side was designated a specific label to tell them apart and identify their orientation in the build. Part orientation is a significant contributor to the amount of swelling that occurs in the green part. At the bottom of Table D.1 are the overall results of the measurements. The average of all of the measurements is displayed. Each measurement was performed twice but in a random order and then averaged. Table D.2 is a second table with the same measurements for a different block.

Table D.1: Measurement for green slotted-cube 2_D_S_F

	Length (mm)	Width (mm)				Shrinkage (% diff)	
		Left	Middle	Right		width	76.50
	9.67	1.34	1.56	1.41		length	54.04
	9.63	1.23	1.56	1.36	Ave All Width		
Average	9.65	1.29	1.56	1.39	1.41		

	Length (mm)	Width (mm)				Shrinkage (% diff)	
		Left	Middle	Right		width	58.64
	11.42	2.58	2.33	2.49		length	45.75
	11.37	2.57	2.38	2.54	Ave All Width		
Average	11.39	2.57	2.36	2.52	2.48		

	Length (mm)	Width (mm)				Shrinkage (% diff)	
		Left	Middle	Right		width	64.06
	11.83	2.18	2.26	2.07		length	44.54
	11.46	2.17	2.17	2.08	Ave All Width		
Average	11.65	2.17	2.22	2.08	2.16		

	Length (mm)	Width (mm)				Shrinkage (% diff)	
		Left	Middle	Right		width	63.33
	11.38	2.19	2.30	2.29		length	45.87
	11.35	1.90	2.25	2.26	Ave All Width		
Average	11.37	2.05	2.28	2.28	2.20		

Slot Shrinkage

	Designed size		Average across part
Width	6	mm	65.63
Length	21	mm	47.55

Table D.2: Measurements for the green slotted-cube 2_D_S_R

	Length (mm)	Width (mm)				Shrinkage (% diff)	
		Left	Middle	Right		Width	70.36
	10.34	1.77	1.79	1.77		Length	50.85
	10.31	1.72	1.82	1.79	Avg All Width		
Average	10.32	1.75	1.81	1.78	1.78		

	Length (mm)	Width (mm)				Shrinkage (% diff)	
		Left	Middle	Right		Width	73.12
	10.93	1.60	1.52	1.70		Length	47.57
	11.09	1.57	1.54	1.75	Avg All Width		
Average	11.01	1.58	1.53	1.73	1.61		

	Length (mm)	Width (mm)				Shrinkage (% diff)	
		Left	Middle	Right		Width	69.10
	12.42	1.76	1.84	2.00		Length	40.87
	12.42	1.74	1.80	1.98	Avg All Width		
Average	12.42	1.75	1.82	1.99	1.85		

	Length (mm)	Width (mm)				Shrinkage (% diff)	
		Left	Middle	Right		width	68.68
	11.25	1.88	1.79	1.93		length	46.79
	11.10	1.83	1.98	1.88	Avg All Width		
Average	11.17	1.85	1.88	1.90	1.88		

	Designed size			Avg. shrinkage across part	
	Width	6	mm	70.32	%
	Length	21	mm	46.52	%

APPENDIX E.
RAW DATA FOR SINTERED SLOT VARIATION

Results for the block labeled as 2D_S_F_S are shown in Table E.1. This is the sintered block of 2D_S_F. The different faces that have slots on them are separated into different sections (to match Table D.1). Table E.2 has the same information as E.1 but for a different slotted-cube – 2D_S_R_S. This is the sintered 2D_S_R.

Table E.1: Variation for sintered and green slotted-cube 2D_S_F

	Length (mm)	Width (mm)			
		Left	Middle	Right	
	7.18	2.02	2.29	2.35	
	7.14	2.10	2.32	2.36	Ave All Width (mm)
Average (mm)	7.16	2.06	2.31	2.35	2.24

	Length (mm)	Width (mm)			
		Left	Middle	Right	
	7.46	2.38	2.50	2.53	
	7.36	2.41	2.46	2.53	Ave All Width (mm)
Average (mm)	7.41	2.40	2.48	2.53	2.47

	Length (mm)	Width (mm)			
		Left	Middle	Right	
	10.74	1.59	1.01	1.00	
	10.78	1.55	1.03	0.92	Ave All Width (mm)
Average (mm)	10.76	1.57	1.02	0.96	1.18

	Length (mm)	Width (mm)			
		Left	Middle	Right	
	9.22	2.09	2.30	2.32	
	9.30	2.23	2.32	2.37	Ave All Width (mm)
Average (mm)	9.26	2.16	2.31	2.34	2.27

Table E.2: Variation for sintered sand green slotted-cube 2D_S_R

	Length (mm)	Width (mm)			
		Left	Middle	Right	
	11.03	1.74	1.84	1.80	
	10.57	1.68	1.83	1.78	Ave All Width (mm)
Average (mm)	10.80	1.71	1.83	1.79	1.78

	Length (mm)	Width (mm)			
		Left	Middle	Right	
	12.78	2.44	2.62	2.59	
	12.29	2.46	2.58	2.60	Ave All Width (mm)
Average (mm)	12.53	2.45	2.60	2.60	2.55

	Length (mm)	Width (mm)			
		Left	Middle	Right	
	13.06	2.12	2.26	1.76	
	12.98	2.07	2.13	1.89	Ave All Width (mm)
Average (mm)	13.02	2.09	2.20	1.83	2.04

	Length (mm)	Width (mm)			
		Left	Middle	Right	
	11.75	1.88	2.25	2.04	
	11.51	1.89	1.91	1.85	Ave All Width (mm)
Average (mm)	11.63	1.88	2.08	1.94	1.97

APPENDIX F.

RAW DATA FOR SURFACE ROUGHNESS MEASUREMENTS

The data presented in this appendix are the measurements of the surface roughness for several flexural test bars. The bars were numbers for identification. All values are for sintered bars. The green bars were made from SLS of the stearic acid/alumina powder. The total average (Total Avg.) given in the most right-hand column is the average of every side's surface roughness. The average of each individual side (Side Avg.) is also presented. The top and bottom side labeling corresponds with the part orientation in the build, i.e. the bottom side was the bottom of the part as produced in the SLS machine. Side 1 and side 2 are relative to the end of the bar that is numbered. Side 1 is the right side of the bar when the identification number on the bar is up and nearest the hand. This position is demonstrated in Figure F.1.

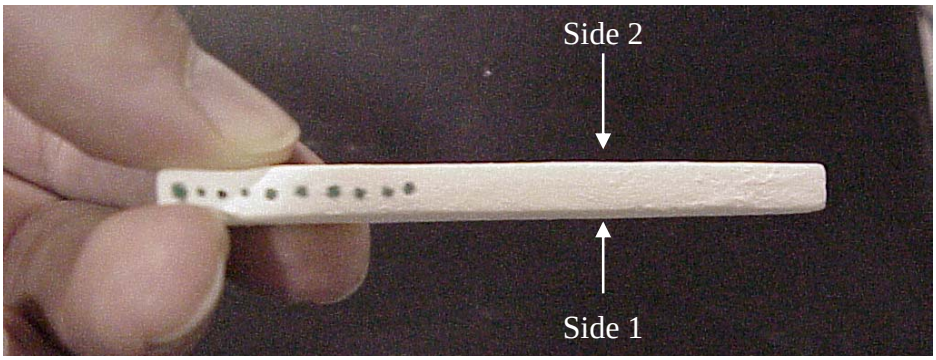

Figure F.1: Bar position for distinguishing side 1 from side 2

Table F.1: Surface roughness data (μm) for sintered test bars

#2 Bar Curved End					
Side	Left	Middle	Right	Side Avg.	Total Avg.
Bottom	4.77	6.09	6.57	5.81	**6.41**
1	6.96	6.22	7.73	6.97	
2	6.27	5.39	5.49	5.72	
Top	7.36	5.81	8.23	7.13	
#3 Bar					
Side	Left	Middle	Right	Side Avg.	Total Avg.
Bottom	4	3.32	3.55	3.62	**6.25**
1	5.91	5.97	11.91	7.93	
2	5.97	5.7	7.71	6.46	
Top	6	8.18	6.72	6.97	
#4 Bar					
Side	Left	Middle	Right	Side Avg.	Total Avg.
Bottom	6.33	5.57	5.26	5.72	**9.16**
1	9.77	11.98	13.7	11.82	
2	5.91	5.62	7.84	6.46	
Top	14.49	9.57	13.92	12.66	
#5 Bar					
Side	Left	Middle	Right	Side Avg.	Total Avg.
Bottom	6.94	3.64	5.11	5.23	**7.11**
1	6.3	5.8	10.61	7.57	
2	9.07	5.64	8.26	7.66	
Top	8.21	7.69	8.1	8.00	
#7 Bar					
Side	Left	Middle	Right	Side Avg.	Total Avg.
Bottom	6.89	6.08	6.01	6.33	**8.10**
1	6.5	11.98	6.06	8.18	
2	6.88	6.7	6.24	6.61	
Top	13.77	10.36	9.75	11.29	
#8 Bar					
Side	Left	Middle	Right	Side Avg.	Total Avg.
Bottom	5.75	4.36	9.62	6.58	**7.47**
1	12.78	5.78	6.81	8.46	
2	9.14	6.36	5.59	7.03	
Top	9.91	6.22	7.32	7.82	
#10 Bar					
Side	Left	Middle	Right	Side Avg.	Total Avg.
Bottom	6.41	5.51	9.13	7.02	**8.08**
1	6.96	5.96	7.23	6.72	
2	11.19	7.07	5.47	7.91	
Top	7.13	11.68	13.25	10.69	

Side	Left	Middle	Right	Side Avg.	Total Avg.
Bottom	10.96	6.24	9.46	8.89	**8.43**
1	18.97	5.79	5.54	10.10	
2	6.21	6.88	7.2	6.76	
Top	11.31	5.42	7.15	7.96	

APPENDIX G.

DATA FOR ANGLED HOLE VARIATION MEASUREMENTS

This information was collected from the green hole bars to study the effect of orientation angle from vertical on the diameter of holes. Rotation of parts is one way reduce the severity of bulging in a part, but the greater the part rotation form vertical, the greater the hole reduction in diameter. Table G.1 shows the information used to confirm this observation. Both the upper and lower surfaces of the holes were analyzed and the measurements were repeated in a random order to help validate the results. Table G.2 shows same information for parts with holes in line with the vertical axis (i.e. blocks "90° from vertical") and perpendicular to it (i.e. "0° from vertical"). This is the clearest indicator of how much effect part orientation has on hole diameter.

Table G.1: Hole reductions at various angles from vertical

Reductions in hole diameters of rotated green hole bars									
		Left		Mid Left		Mid Right		Right	
	Part # (U/L)	(mm)	(%)	(mm)	(%)	(mm)	(%)	(mm)	(%)
30 degrees from vert.	1U	1.67	33.33	1.72	34.35	1.73	34.64	1.67	33.42
	1L	1.42	28.33	1.06	21.24	1.32	26.48	1.27	25.42
	2U	1.53	30.57	1.58	31.60	1.50	30.07	1.40	28.01
	2L	1.30	26.09	1.58	31.65	1.72	34.36	1.58	31.52
	3U	1.44	28.85	1.41	28.15	1.26	25.17	1.01	20.14
	3L	1.88	37.60	1.90	37.95	1.75	34.97	1.89	37.80
45 degrees from vert.	4U	1.68	33.57	5.00	100.00	1.62	32.44	5.00	100.00
	4L	1.33	26.67	5.00	100.00	1.34	26.79	5.00	100.00
	16U	1.39	27.80	5.00	100.00	1.52	30.36	5.00	100.00
	16L	1.93	38.65	5.00	100.00	2.09	41.85	5.00	100.00
	17U	1.34	26.86	5.00	100.00	1.43	28.58	5.00	100.00
	17L	1.86	37.14	5.00	100.00	1.93	38.53	5.00	100.00
60 degrees from vert.	9U	2.00	40.01	1.80	36.08	1.84	36.77	1.93	38.58
	9L	1.97	39.50	1.91	38.21	1.76	35.21	1.18	23.61
	11U	2.13	42.62	2.06	41.13	2.07	41.41	2.17	43.34
	11L	2.01	40.16	1.93	38.58	2.07	41.31	2.15	42.93
	14U	2.03	40.52	5.00	100.00	1.89	37.90	5.00	100.00
	14L	2.07	41.41	5.00	100.00	2.22	44.46	5.00	100.00

Table G.2: Hole diameter reductions in bars at 0° and 90°

		Variation in hole diameters of rotated green hole bars							
		Left		Mid Left		Mid Right		Right	
	Part # (U/L)	(mm)	(%)	(mm)	(%)	(mm)	(%)	(mm)	(%)
0 degrees from vert.	3U	2.30	46.09	2.50	100.00	2.43	48.52	2.50	100.00
	3L	2.30	46.08	2.50	100.00	2.29	45.77	2.50	100.00
	11U	2.08	41.53	2.50	100.00	2.53	50.51	2.50	100.00
	11L	2.28	45.51	2.50	100.00	2.62	52.38	2.50	100.00
	9U	2.03	40.67	2.10	41.99	2.34	46.85	2.39	47.76
	9L	2.25	45.06	2.06	41.30	2.36	47.27	2.71	54.15
	17U	2.07	41.33	1.93	38.70	2.08	41.52	2.11	42.22
	17L	2.07	41.38	1.93	38.50	2.35	46.93	2.83	56.62
90 degrees from vert.	6U	1.29	25.81	1.37	54.77	1.21	24.26	1.42	56.97
	6L	1.45	29.05	1.43	57.03	1.29	25.86	1.42	56.67
	10U	1.49	29.70	1.38	27.62	1.42	28.39	1.41	28.27
	10L	1.46	29.21	1.39	27.83	1.60	31.96	1.85	36.97
	12U	1.24	24.84	1.44	57.61	1.35	26.92	1.80	71.87
	12L	1.20	23.91	1.46	58.48	1.28	25.63	1.40	56.10
	16U	1.58	31.54	1.56	31.21	1.57	31.45	1.98	39.57
	16L	1.54	30.81	1.43	28.56	1.48	29.61	1.72	34.44

BIBLIOGRAPHY

1. Ahn, S., Lee, C.S., Jeong, W., "Development of Translucent FDM Parts by Post-Processing," *Rapid Prototyping Journal*, Vol. 10 [4], pp. 218-224, 2004.

2. Bourell, D., Beaman, J., Stevinson, B., "Support-Free Infiltration of Selective Laser Sintered (SLS) Non-metallic Preforms," *Proceedings of NSF Design, Service, and Manufacturing Grantees and Research Conference, St. Louis, MO,* 2006.

3. Friedel, T., Travitzky, N., Nielbling, F., Scheddler, M., Greil, P., "Fabrication of Polymer Derived Ceramic Parts by Selective Laser Curing," *Journal of European Ceramic Society*, Vol. 25, pp. 193-197, 2005.

4. Dhara, S., Su, B., "Green Machining to Net Shape Alumina Ceramics Prepared Using Different Processing Routes," *International Journal of Applied Ceramic Technology*, Vol. 2 [3], pp. 262-270, 2005.

5. Gahler, A., Heinrich, J.G., Günster, J., "Direct Laser Sintering of Al_2O_3-SiO_2 Dental Ceramic Components by Layer-Wise Slurry Deposition," *Journal of American Ceramic Society*, Vol. 89 [10], pp. 3076-3080, 2006.

6. Gill, T., Hon, B., "Selective Laser Sintering of SiC/Polyamide Matrix Composites," *Proceedings of Solid Freeform Fabrication Symposium*, August 5-7, Austin, TX, pp. 538-545, 2002.

7. Guo, D., Cai, K., Nan, C., Long-tu, L., Gui, Z., "Rapid Prototyping of Piezoelectric Ceramics via Selective Laser Sintering and Gelcasting," *Journal of the American Ceramic Society*, Vol. 87 [1], pp. 17-22, 2004.

8. Hao, L., Lawrencea, J., Lowb, D.K.Y., Limb, G.C., Zhen, H.Y., "Correlation of the Hydroxyl Bond and Wettability Characteristics of a Magnesia Partially Stabilised Zirconia Following CO2 Laser Irradiation," *Thin Solid Films*, Vol. 468, pp. 12-16, 2004.

9. Harlan, N., Park, S., Bourell, D. L., Beaman, J., J., "Selective Laser Sintering of Zirconia with Micro-Scale Features," *Proceedings of Solid Freeform Fabrication Symposium*, August, Austin, TX, pp. 297-302, 1999.

10. Haung, T., Mason, M.S., Hilams, G.E., Leu, M.C., "Freeze-form Extrusion Fabrication of Ceramics," *Proceedings of Solid Freeform Fabrication Symposium*, August 1-3, Austin, TX, 2005.

11. King, A.G., Chapter 10, *Ceramic Technology and Processing*, Noyes Publications, 2002.

12. Kumar, V., Khamba, J. S., "Experimental Investigation of Ultrasonic Machining of an Alumina-Based Ceramic Composite," *Journal of the American Ceramic Society*, Vol. 89 [8], pp. 2413-2417, 2006.

13. Licciulli, A., Greco, A., Maffezzoli, A., "Development of a Pro-Ceramic Suspension for Freeform Fabrication of Ceramic Parts by Stereolithography," *Journal of Industrial Ceramics* Vol. 20 [2], pp. 97-99, 2000.

14. Löschau, W., Lenk, R., Teichgräber, M., Nowotny, S., Richter, C., "Prototyping of Complex-Si/SiC-Ceramics by Selective Laser Sintering," *Journal of Industrial Ceramics* Vol. 20 [2], pp. 95-96, 2000.

15. Mason, M.S., Haung, T., Landers, R.G., Leu, M.C., Hilmas, G.E., "Freeform Extrusion of High Solids Loading Ceramic Slurries, Part I: Extrusion Process Modeling," *Proceedings of Solid Freeform Fabrication Symposium*, August 14-16, Austin, TX, 2006.

16. Muttamara, A., Fukuzawa, Y., Mohri, N., Tani, T., "Probability of Precision Micro-Machining of Insulating Si_3N_4 Ceramics by EDM," *Journal of Material Processing Technologies* Vol. 140, pp. 243-247, 2003.

17. Nelson, J.C., Vail, N.K., Barlow, J.W., Beaman, J.J., Bourell, D.L., and Marcus, H.L., "Selective Laser Sintering of Polymer-Coated Silicon Carbide Powder," *Industry & Engineering Chemistry Research*, Vol. 34, pp. 1641-1651, 1995.

18. Rahaman, M.N., Chapter 7 & Appendix E, *Ceramic Processing and Sintering*, Second edition, Taylor & Francis, 2003.

19. Reddy, T. A. J., Kumar, Y. R., Rao, C. S. P., "Determination of Optimum Process Parameters Using Taguchi's Approach to Improve the Quality of SLS Parts," *Proceedings of the 17th IASTED International Conference*, May 24-26, Montreal, QC, Canada, 2006.

20. Song, J.H., Evans, J.R.G., "On the Machinability of Ceramic Compacts," *Journal of European Ceramic Society*, Vol. 17 [14], pp. 1665-1673, 1997.

21. Stierlen, P., Schanz, P., Eyerer, P., "Si/SiC - Ceramic Low Process Shrinkage - High Temperature Material for the Laser Sinter Process," *Proceedings of Solid Freeform Fabrication Symposium*, August 11-13, Austin, TX, pp. 581-588, 1998.

22. Subramanian, P.K., Barlow, J.W., Marcus, H.L., "Effect of Particle Size on SLS and Post-Processing of Alumina with Polymer Binders," *Proceedings of Solid Freeform Fabrication Symposium*, August 7-9, Austin, TX, pp. 346-352, 1995.

23. Tong, K., Lehtihet, E.A., Joshi, S., "Parametric Error Modeling and Software Error Compensation for Rapid Prototyping," *Rapid Prototyping Journal*, Vol. 9 [5], pp.301-313, 2003

24. Vaidyanathan, R., Walish, J., Lombardi, J.L., S. Kasichainula, Calvert, P., Cooper, K.C., "The Extrusion Freeforming of Functional Ceramic Prototypes", *Journal of Material*, Vol. 52 [12], pp. 34-37, 2000.

25. Wang, J., Shaw, L.L., "Solid Freeform Fabrication of Permanent Dental Restorations via Slurry Micro-Extrusion," *Journal of American Ceramic Society*, Vol. 89 [1], pp. 346-349, 2006.

26. CIM process, http://www.smallprecisiontools.com/index.cfm?fuseaction=show&temp=default&parents_id=438, Feb. 27, 2007.

27. Data sheet of Reactive Aluminas for Ceramic Applications from Almatis – grade A-16SG, http://www.almatis.com/download/data-sheets/GP-RCP_008_Ceramics.pdf, Mar. 13, 2008.

28. FDM operation diagram, http://www.xpress3d.com/FDM.aspx, Feb. 26, 2007.

29. Properties of an 85% vitreous alumina part, http://www.matweb.com/search/SpecificMaterial.asp?bassnum=BA2C, Mar. 13, 2007.

30. Properties of a 99.9% alumina part, http://www.matweb.com/search/SpecificMaterial.asp?bassnum=BA1A, Mar. 13, 2007.

31. SLA part examples, http://www.matrixenterprises.com/slaprot.htm, Feb. 27, 2007.

32. Slip casting, http://www.abcir.org/slip.shtml, Mar. 18, 2007.

33. SLS operation diagram, http://www.msoe.edu/rpc/graphics/sls_process.jpg, Mar. 18, 2007.

34. Tape casting, http://www.keram.se/eng/pdf/tejp_eng.pdf, Feb. 27, 2007.

VITA

Jason Nolte was born on May 13th, 1984, Mother's Day, in Memphis, Tennessee. He received his primary and secondary education in Memphis where he graduated from Germantown High School in May of 2002. In August of 2002, he enrolled in the University of Missouri – Rolla (UMR), and graduated Magna Cum Laude with a B.S. degree in Mechanical Engineering with honors in December of 2005. He began his work as a master's student under the direction Dr. Ming Leu at UMR the following semester. He graduated in May of 2007 with a M.S. degree in Mechanical Engineering.

While enrolled at the UMR, Jason participated in several organizations, the primary of which were the band and the solar car team. In band, Jason played the alto and soprano saxophone in jazz, concert, and marching band. He played as first chair alto saxophone in both the concert and jazz band. Jason's involvement in the solar car team included being a driver in the 2003 North American Solar Challenge, in which the team finished first in the race from Chicago, IL to Los Angeles, CA along Route 66. He enjoyed working with other team members to design, analyze, and validate the mechanical systems of the car, including the chassis, suspension, wheels, and body. He also served the team as Director of Fundraising, Vice President of Business Operations, and President of the team during his time at UMR. Jason is also a member of the engineering honor societies Tau Beta Pi and Pi Tau Sigma.

Jason has enjoyed his time at UMR, and is looking forward to what the future has in-store for him and his lovely wife. He is confident that his education has well prepared him for whatever professional challenges may arise.